Monthly Notices
of the
ROYAL ASTRONOMICAL SOCIETY

MNRAS **435,** 861–878 (2013)
Advance Access publication 2013 August 22

doi:10.1093/mnras/stt1356

The UVES large program for testing fundamental physics – II. Constraints on a change in μ towards quasar HE 0027−1836⋆

H. Rahmani,[1]† M. Wendt,[2,3] R. Srianand,[1] P. Noterdaeme,[4] P. Petitjean,[4] P. Molaro,[5,6] J. B. Whitmore,[7] M. T. Murphy,[7] M. Centurion,[5] H. Fathivavsari,[8] S. D'Odorico,[9] T. M. Evans,[7] S. A. Levshakov,[10,11] S. Lopez,[12] C. J. A. P. Martins,[6] D. Reimers[2] and G. Vladilo[5]

[1]*Inter-University Centre for Astronomy and Astrophysics, Post Bag 4, Ganeshkhind, Pune 411 007, India*
[2]*Hamburger Sternwarte, Universität Hamburg, Gojenbergsweg 112, D-21029 Hamburg, Germany*
[3]*Institut für Physik und Astronomie, Universität Potsdam, D-14476 Golm, Germany*
[4]*Institut d'Astrophysique de Paris, CNRS-UMPC, UMR7095, 98bis Bd Arago, F-75014 Paris, France*
[5]*INAF-Osservatorio Astronomico di Trieste, Via G. B. Tiepolo 11, I-34131 Trieste, Italy*
[6]*Centro de Astrofísica, Universidade do Porto, Rua das Estrelas, P-4150-762 Porto, Portugal*
[7]*Centre for Astrophysics and Supercomputing, Swinburne University of Technology, Hawthorn, VIC 3122, Australia*
[8]*Department of Theoretical Physics and Astrophysics, University of Tabriz PO Box 51664, Tabriz, Iran*
[9]*ESO, Karl Schwarzschild-Str. 1, D-85748 Garching, Germany*
[10]*Ioffe Physical-Technical Institute, Polytekhnicheskaya, Str. 26, 194021 Saint Petersburg, Russia*
[11]*St Petersburg Electrotechnical University 'LETI', Prof. Popov Str. 5, 197376 St Petersburg, Russia*
[12]*Departamento de Astronomia, Universidad de Chile, Casilla 36-D, Santiago, Chile*

Accepted 2013 July 19. Received 2013 July 19; in original form 2013 May 25

ABSTRACT

We present an accurate analysis of the H_2 absorption lines from the $z_{abs} \sim 2.4018$ damped Lyα system towards HE 0027−1836 observed with the Very Large Telescope Ultraviolet and Visual Echelle Spectrograph (VLT/UVES) as a part of the European Southern Observatory Large Programme 'The UVES large programme for testing fundamental physics' to constrain the variation of proton-to-electron mass ratio, $\mu \equiv m_p/m_e$. We perform cross-correlation analysis between 19 individual exposures taken over three years and the combined spectrum to check the wavelength calibration stability. We notice the presence of a possible wavelength-dependent velocity drift especially in the data taken in 2012. We use available asteroids spectra taken with UVES close to our observations to confirm and quantify this effect. We consider single- and two-component Voigt profiles to model the observed H_2 absorption profiles. We use both linear regression analysis and Voigt profile fitting where $\Delta\mu/\mu$ is explicitly considered as an additional fitting parameter. The two-component model is marginally favoured by the statistical indicators and we get $\Delta\mu/\mu = -2.5 \pm 8.1_{stat} \pm 6.2_{sys}$ ppm. When we apply the correction to the wavelength-dependent velocity drift, we find $\Delta\mu/\mu = -7.6 \pm 8.1_{stat} \pm 6.3_{sys}$ ppm. It will be important to check the extent to which the velocity drift we notice in this study is present in UVES data used for previous $\Delta\mu/\mu$ measurements.

Key words: intergalactic medium – quasars: absorption lines – quasars: individual: HE 0027−1836.

1 INTRODUCTION

Fundamental theories in physics rely on a set of free parameters whose values have to be determined experimentally and cannot be calculated on the basis of our present knowledge of physics. These free parameters are called fundamental constants as they are assumed to be time and space independent in the simpler of the successful physical theories (see Uzan 2011, and references therein). The fine structure constant, $\alpha \equiv e^2/\hbar c$, and the proton-to-electron mass ratio, μ, are two such dimensionless constants that are more straightforward to be measured experimentally. Current laboratory measurements exclude any significant variation of these dimensionless constants over Solar system scales and on geological time-scales (see Olive & Skillman 2004; Petrov et al. 2006; Rosenband et al. 2008; Shelkovnikov et al. 2008). However, it is

⋆ Based on data obtained with UVES at the VLT of the European Southern Observatory (Prgm. ID 185.A-0745).
† E-mail: hadi@iucaa.ernet.in

neither observationally nor experimentally excluded that these fundamental constants could vary over cosmological distances and time-scales. Therefore, constraining the temporal and spatial variations of these constants can have a direct impact on cosmology and fundamental physics (Amendola et al. 2012; Ferreira et al. 2012).

It is known that the wavelengths of the rovibronic molecular transitions are sensitive to μ. In a diatomic molecule, the energy of the rotational transitions is proportional to the reduced mass of the molecule, M, and that of vibrational transitions is proportional to $\sqrt{M}$, in the first-order approximation. The frequency of the rovibronic transitions in Born–Oppenheimer approximation can be written as

$$\nu = c_{\rm elec} + c_{\rm vib}/\sqrt{\mu} + c_{\rm rot}/\mu, \quad (1)$$

where $c_{\rm elec}$, $c_{\rm vib}$ and $c_{\rm rot}$ are some numerical coefficients related, respectively, to electronic, vibrational and rotational transitions. Therefore, by comparing the wavelength of the molecular transitions detected in quasar spectra with their laboratory values one can measure the variation in μ (i.e. $\Delta\mu/\mu \equiv (\mu_z - \mu_0)/\mu_0$ where μ_z and μ_0 are the values of proton-to-electron mass ratio at redshift z and today) over cosmological time-scales. Using intervening molecular absorption lines seen in the high-z quasar spectra for measuring $\Delta\mu/\mu$ in the distant universe was first proposed by Thompson (1975). As H_2 is the most abundant molecule, its Lyman and Werner absorption lines seen in the quasar absorption spectra have been frequently used to constrain the variation of μ. However, H_2 molecules are detected in only a few per cent of the high-redshift damped Lyman α (DLA) systems (Petitjean, Srianand & Ledoux 2000; Ledoux, Petitjean & Srianand 2003; Noterdaeme et al. 2008; Srianand et al. 2012; Jorgenson et al. 2013) with only a handful of them being suitable for probing the variation of μ (see Petitjean et al. 2009).

If μ varies, the observed wavelengths of different H_2 lines will shift differently with respect to their expected wavelengths based on laboratory measurements and the absorption redshift. The sensitivity of the wavelength of the ith H_2 transition to the variation of μ is generally parametrized as

$$\lambda_i = \lambda_i^0(1 + z_{\rm abs})\Big(1 + K_i \frac{\Delta\mu}{\mu}\Big), \quad (2)$$

where λ_i^0 is the rest-frame wavelength of the transition, λ_i is the observed wavelength, K_i is the sensitivity coefficient of ith transition and $z_{\rm abs}$ is the redshift of the H_2 absorber. Alternatively, equation (2) can be written as

$$z_i = z_{\rm abs} + C K_i, \quad C = (1 + z_{\rm abs})\frac{\Delta\mu}{\mu}, \quad (3)$$

which clearly shows that $z_{\rm abs}$ is only the mean redshift of transitions with $K_i = 0$. Equation (3) is sometimes presented as

$$z_{\rm red} \equiv \frac{(z_i - z_{\rm abs})}{(1 + z_{\rm abs})} = K_i \frac{\Delta\mu}{\mu} \quad (4)$$

that shows the value of $\Delta\mu/\mu$ can be determined using a linear regression analysis of reduced redshift ($z_{\rm red}$) versus K_i. This method has been frequently used in the literature for constraining the variation of μ (see Varshalovich & Levshakov 1993; Cowie & Songaila 1995; Levshakov et al. 2002; Ivanchik et al. 2005; Reinhold et al. 2006; Ubachs et al. 2007; Thompson et al. 2009a; Wendt & Molaro 2011, 2012). However, at present, measurements of $\Delta\mu/\mu$ using H_2 is limited to six H_2-bearing DLAs at $z \geq 2$. All of these analyses suggest that $|\Delta\mu/\mu| \leq 10^{-5}$ at $2 \leq z \leq 3$. The best reported constraints based on a single system being $\Delta\mu/\mu = +(0.3 \pm 3.7) \times 10^{-6}$ reported by King et al. (2011) towards Q0528−250.

At $z \leq 1.0$, a stringent constraint on $\Delta\mu/\mu$ is obtained using inversion transitions of NH_3 and rotational molecular transitions (Murphy et al. 2008; Henkel et al. 2009; Kanekar 2011). The best reported limit using this technique is $\Delta\mu/\mu = -(3.5 \pm 1.2) \times 10^{-7}$ (Kanekar 2011). Bagdonaite et al. (2013) obtained the strongest constraint to date of $\Delta\mu/\mu = (0.0 \pm 1.0) \times 10^{-7}$ at $z = 0.89$ using methanol transitions. However, $\Delta\mu/\mu$ measurements using NH_3 and CH_3OH are restricted to only two specific systems at $z \leq 1$. Alternatively, one can place good constraints using 21-cm absorption in conjunction with metal lines and assuming all other constants have not changed (see for example Tzanavaris et al. 2007). Rahmani et al. (2012) have obtained $\Delta\mu/\mu = (0.0 \pm 1.50) \times 10^{-6}$ using a well-selected sample of four 21-cm absorbers at $z_{\rm abs} \sim 1.3$. Srianand et al. (2010) have obtained $\Delta\mu/\mu = (-1.7 \pm 1.7) \times 10^{-6}$ at $z \sim 3.17$ using the 21-cm absorber towards J1337+3152. However, one of the main systematic uncertainties in this method comes from how one associates 21-cm and optical absorption components. More robust estimates can be obtained from observations of microwave and submillimetre molecular transitions of the same molecule which have different sensitivities to μ-variations (for a review, see Kozlov & Levshakov 2013).

Here, we report a detailed analysis of H_2] absorption in $z = 2.4018$ DLA towards HE 0027−1836 (Noterdaeme et al. 2007) using the Ultraviolet and Visual Echelle Spectrograph mounted on the Very Large Telescope (VLT/UVES) spectra taken as part of the UVES large programme for testing the fundamental physics (Molaro et al. 2013).

2 OBSERVATION AND DATA REDUCTION

HE 0027−1836 (UM 664) with a redshift $z_{\rm em} = 2.55$ and an r-band magnitude of 18.05 was discovered by MacAlpine & Feldman (1982) as part of their search for high-redshift quasars. The optical spectroscopic observations of HE 0027−1836 were carried out using VLT/UVES (Dekker et al. 2000) Unit Telescope (UT2) 8.2-m telescope at Paranal (Chile) [as part of ESO Large Programme 185.A-0745 '*The UVES Large Program for testing Fundamental Physics*' (Molaro et al. 2013)]. All observations were performed using the standard beam splitter with the dichroic 2 (setting 390+580) that covers roughly from 330 to 450 nm on the BLUE CCD and from 465 to 578 nm and from 583 to 680 nm on the two RED CCDs. A slit width of 0.8 arcsec and CCD readout with no binning were used for all the observations, resulting in a pixel size of ≈1.3–1.5 km s^{-1} on the BLUE CCD and spectral resolution of ≈60 000. All the exposures were taken with the slit aligned with the parallactic angle to minimize the atmospheric dispersion effects. The observations are comprised of 19 exposures totalling 33.3 h of exposure time in three different observing cycles started in 2010 and finished in 2012. The amount of observing time in different cycles are, respectively, 10.4, 12.5 and 10.4 h for the first, second and third cycles. Table 1 summarizes the observing date and exposure time along with the seeing and airmass for all the 19 exposures divided into three groups based on observing cycles.

D'Odorico et al. (2000) have shown that the resetting of the grating between an object exposure and the ThAr calibration lamp exposure can result in an error of the order of a few hundred metres per second in the wavelength calibration. To minimize this effect, each science exposure was followed immediately by an attached ThAr lamp exposure. For wavelength calibration of each science

Table 1. Log of the optical spectroscopic observation of HE 0027−1836 with VLT/UVES⋆. Column 5: Seeing at the beginning of the exposure as recorded by Differential Image Motion Monitor (DIMM) at Paranal. Column 6: Airmass at the beginning of the exposure. Column 7: Signal-to-noise ratio (SNR) calculated from a line free region in the observed wavelength range 3786–3795 Å. Column 8: The mean velocity difference between the clean H_2 lines with observed wavelengths larger and smaller than 3650 Å.

Exposure identification (1)	Observing date (2)	Starting time (UT) (3)	Exposure (s) (4)	Seeing (arcsec) (5)	Airmass (6)	SNR (7)	Δv (km s^{-1}) (8)
		cycle 1 : 2010					
EXP01	2010-07-13	07:59:03.56	6250	0.68	1.11	9.04	+0.16
EXP02	2010-07-15	07:46:52.45	6250	0.81	1.12	8.22	+0.47
EXP03	2010-08-09	06:33:45.04	6250	0.55	1.07	11.23	+0.62
EXP04	2010-08-10	07:06:48.37	6250	0.65	1.02	9.13	+0.36
EXP05	2010-08-19	07:45:02.18	6250	0.82	1.01	10.49	+0.23
EXP06	2010-10-05	01:22:39.57	6250	1.04	1.32	7.56	+0.40
		cycle 2 : 2011					
EXP07	2011-10-31	02:30:27.36	6400	1.01	1.01	8.35	+0.30
EXP08	2011-10-31	04:20:34.65	6400	1.28	1.10	8.38	+0.30
EXP09	2011-11-01	02:10:20.43	6400	0.72	1.01	9.04	+0.42
EXP10	2011-11-02	01:57:51.97	6400	1.05	1.01	8.64	−0.20
EXP11	2011-11-03	02:03:07.21	6400	1.02	1.01	8.66	+0.36
EXP12	2011-11-04	00:36:35.75	6400	1.63	1.10	8.02	+0.63
EXP13	2011-11-04	02:33:35.34	6700	1.27	1.01	9.35	+0.58
		cycle 3 : 2012					
EXP14	2012-07-16	08:19:06.35	6250	0.73	1.06	8.21	+0.56
EXP15	2012-07-25	07:34:12.34	6250	0.66	1.07	10.25	+0.49
EXP16	2012-08-14	06:22:02.87	6250	0.66	1.06	10.19	+0.68
EXP17	2012-08-16	05:57:14.67	6250	0.79	1.09	7.73	+0.80
EXP18	2012-08-16	07:54:15.53	6250	1.00	1.01	6.58	+0.57
EXP19	2012-08-22	07:37:54.22	6250	0.55	1.01	9.93	+0.35

⋆All the exposure are taken using 390+580 setting with no binning for CCD readout and slit aligned to the parallactic angle.

exposure, we use the attached mode ThAr frame just taken after it. The data were reduced using UVES Common Pipeline Library (CPL) data reduction pipeline release 5.3.1[1] using the optimal extraction method. We used fourth-order polynomials to find the dispersion solutions. The number of suitable ThAr lines used for wavelength calibration was usually more than 700 and the rms error was found to be in the range 40–50 m s^{-1} with zero average. However, this error reflects only the calibration error at the observed wavelengths of the ThAr lines that are used for wavelength calibration. The systematic errors affecting the wavelength calibration should be measured by other techniques that will be discussed later in the paper.

To avoid rebinning of the pixels we use the final un-rebinned extracted spectrum of each order produced by CPL. We apply the CPL wavelength solutions to each order and merge the orders by implementing a weighted mean in the overlapping regions. All the spectra are corrected for the motion of the observatory around the barycenter of the Sun–Earth system. The velocity component of the observatory's barycentric motion towards the line of sight to the quasar was calculated at the exposure mid-point. Conversion of air to vacuum wavelengths was performed using the formula given in Edlén (1966). For the co-addition of the different exposures, we interpolated the individual spectra and their errors to a common wavelength array (while conserving the pixel size) and then computed the weighted mean using weights estimated from the errors in each pixel. The typical signal-to-noise ratio (SNR) measured in a line free region of 3786–3795 Å is given in the seventh column of Table 1. We notice that our final combined spectrum has an SNR of ∼29 at this wavelength interval.

[1] http://www.eso.org/sci/facilities/paranal/instruments/uves/doc/

3 SYSTEMATIC UNCERTAINTIES IN THE UVES WAVELENGTH SCALE

The shortcomings of the ThAr wavelength calibration of quasar spectra taken with VLT/UVES have already been discussed by a number of authors (Chand et al. 2006; Levshakov et al. 2006; Molaro et al. 2008; Thompson et al. 2009b; Whitmore, Murphy & Griest 2010; Agafonova et al. 2011; Wendt & Molaro 2011; Rahmani et al. 2012; Agafonova et al. 2013). The availability of 19 independent spectra taken over a three year period allows us to investigate the presence of any velocity drift as a function of wavelength in our spectra and study its evolution with time before we embark on $\Delta\mu/\mu$ measurements. In the last column of Table 1 we give Δv, the velocity offset based on the mean $z_{\rm abs}$ of H_2 lines detected below and above 3650Å. Ideally, if $\Delta\mu/\mu = 0$, we expect this to distribute randomly around zero. But we notice that apart from one case the values are always positive. Below we use cross-correlation analysis to address this in great detail.

3.1 Cross-correlation analysis

Any systematic velocity offset that may be present between different spectra can be estimated using a cross-correlation technique. Here, we cross-correlate the individual spectra as well as the combined

spectrum of each cycle with respect to the combined spectrum of all 19 exposures in the wavelength windows each typically spread over one echelle order. As we are interested in H_2 lines, we limit this analysis to $3320 < \lambda(\text{Å}) < 3780$ while excluding the wavelength range covered by the very strong Lyβ absorption (i.e. echelle order number 134) of the DLA with $\log N(\text{H I}) \sim 21.7$. The wavelength coverage of each window, which varies between 25 and 31 Å, is large enough to have a couple of saturated- or nearly saturated-absorption lines. This renders the cross-correlation results less sensitive to the photon noise in the low SNR regions of the spectra, thereby increasing the accuracy of such an analysis. We applied the cross-correlation by rebinning each pixel of size $\sim$1.4 km s^{-1} into 20 sub-pixels of size $\sim$ 70 m s^{-1} and measured the offset as the minimum of the χ^2 curve of the flux differences in each window (see Agafonova et al. 2011; Levshakov et al. 2012; Rahmani et al. 2012; Wendt & Molaro 2012, for more detail).

As our cross-correlation analysis implements a rebinning of the spectra on scales of 1/20 of a pixel size and involves very fine interpolations, it should be tested against the possible systematics introduced. To check the accuracy of our cross-correlation analysis, we carried out a Monte Carlo simulation as follows: (1) generate 90 realizations of the combined spectrum in the range of $3750 < \lambda(\text{Å}) < 3780$, with an SNR roughly one-fifth of the combined spectrum to mimic the individual exposures, (2) randomly excluding 25–35 pixels from the realized spectrum to mimic the cosmic ray rejected pixels, (3) applying the same velocity shift to all the 90 realizations and (4) cross-correlating the combined spectrum with each of the 90 spectra to measure the shifts. The filled circles in Fig. 1 show the mean measured shifts from 90 realizations versus the applied shifts for a sample of 100 given shifts uniformly chosen between -400 and 400 m s^{-1}. The residuals, shown as asterisks, have a standard deviation of 6 m s^{-1} and are randomly distributed around the mean of 0 m s^{-1}. The dashed vertical lines in Fig. 1 show the scale of one-tenth of our pixel size. The exercise demonstrates

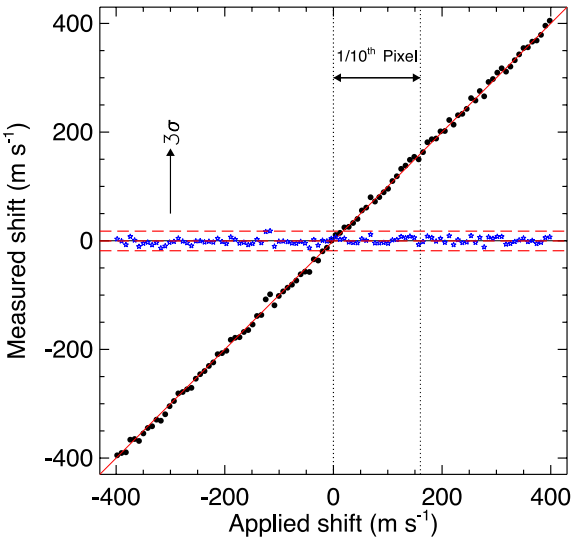

Figure 1. Result of the Monte Carlo simulations to check the validity of our cross-correlation analysis. The abscissa is the applied shift and the ordinate is the mean of the measured shifts for 90 realizations. On the solid line the measured and applied shifts are identical. The asterisks are the residuals (measured minus applied) and the long dashed lines are the mean and 3σ scatter of the residuals. The two vertical dashed lines indicate 1/10th of a pixel size ($\Delta v \sim 0.14$ km s^{-1}).

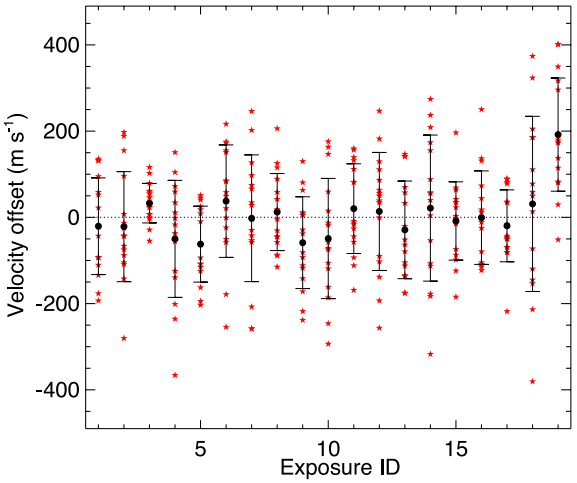

Figure 2. Cross-correlation between the spectrum of different orders in individual exposures and the combined spectrum (see Tables A1–A3 in the appendix). The results of cross-correlation for different orders of each exposure are shown as asterisks. The mean value and 1σ range of the shifts found for each exposure are also shown.

that our method works very well in detecting the sub-pixel shifts between the combined spectra and the individual spectrum.

In Fig. 2, we present the measured velocity offset between the combined spectrum and the individual exposures in m s^{-1} over small wavelength ranges (of size typical of one echelle order). The weighted mean and standard deviation of velocities for each exposure are shown as filled circle and error bar. Apart from exposure 19 (EXP19) all the spectra seem to have average shifts of less than 100 m s^{-1}. In the case of EXP19, the average shift is 195 m s^{-1}. In addition, only one wavelength window has a negative shift and the rest have positive shifts. Therefore, this exposure seems to be severely affected by some systematics. Having a reasonably high SNR, this exposure has already transformed this systematic error to the combined spectrum leading to an erroneous shift estimation. To have a correct estimate of the velocity offsets, we make a combined spectrum after excluding EXP19 and repeat the cross-correlation analysis. Fig. 3 presents the amplitude of the velocity offset in m s^{-1} in different windows for all of the exposures measured with respect to the combined spectrum excluding EXP19. The velocity offsets corresponding to the EXP19 are shown as filled squares. These points have a mean value of 740 m s^{-1}. There also exists a mild trend for the measured shifts of EXP19 to be larger in the red (smaller echelle orders) compared to the blue part (larger echelle orders). We confirm the large velocity shifts in EXP19 using two independent data reductions.

The three cycles of quasar observations are separated by gaps of approximately one year. We next cross-correlate the combined spectrum with that of each cycle to check the stability of the UVES during our observations. The filled circles in different panels of Fig. 4 present the results of this analysis for each cycle. While velocity offsets of the first two cycles show a weak decreasing trend (top two panels of Fig. 4) with increasing wavelength, the last cycle data show a more pronounced trend of velocity offset increasing with increasing wavelength. The filled asterisks in Fig. 4 show the result of similar analysis but after excluding EXP19 both in the total combined spectrum and in the combined spectrum of the third cycle. A careful comparison of the asterisks and circles in the first two cycles shows that for $\lambda \geq 3500$ Å all asterisks have larger values while for $\lambda \leq 3500$ Å they do match. The wavelength-dependent

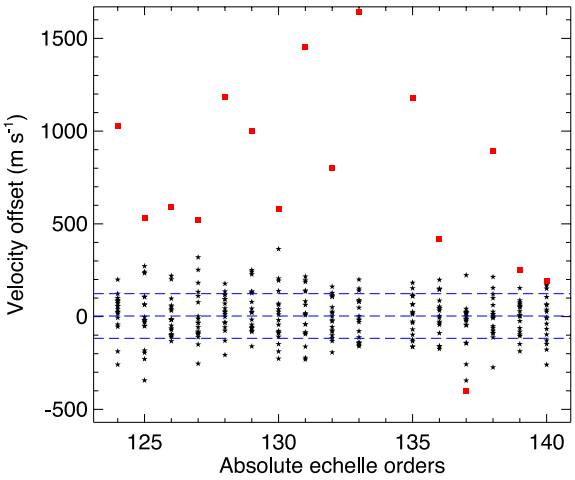

Figure 3. Cross-correlation of individual exposures with the combined spectrum after excluding EXP19. The results of cross-correlation for different orders of each exposure are shown as asterisks. Filled squares show the corresponding velocity offsets measurements for different regions of EXP19. The long dashed lines are marking the mean (3 m s^{-1}) and 1σ (120 m s^{-1}) velocity scatter of the asterisks.

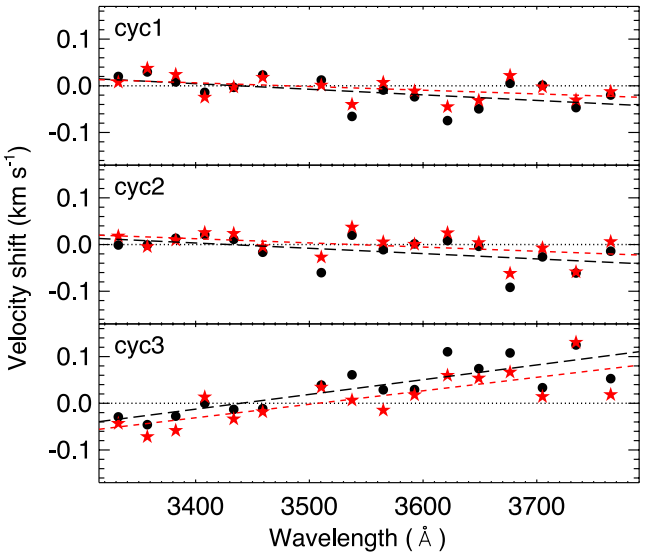

Figure 4. Velocity offsets between the combined spectrum of all exposures and the combined spectrum for each observing cycle. The long dashed lines show the line fitted to these shifts. The asterisks are the results after excluding EXP19 where the short dashed lines show the line fitted to them.

trend in the last cycle has been weakened a bit but still persists even after removing the contribution of EXP19 to the combined spectrum. The exercise shows that in addition to a constant shift there could be a wavelength-dependent drift in EXP19. Further, we also see the indication that even other exposures taken in cycle-3 may have some systematic shift with respect to those observed in previous two cycles. Such trends if real should then be seen in the UVES spectra of the other objects observed in 2012. Probing this will require bright objects where high SNR spectrum can be obtained with short exposure times. Asteroids have been frequently observed with UVES during different cycles and they provide a unique tool for this purpose. We test our prediction about UVES using asteroids in Section 3.2.

3.2 Analysis of the asteroids spectra observed with UVES

The cross-correlation analysis presented above allowed us to detect the regions and/or exposures that have large velocity offsets in comparison to the combined spectrum. However, this exercise is mainly sensitive to detect relative shifts. One needs an absolute wavelength reference with very high accuracy for investigating any absolute wavelength drift in the UVES spectrum. Moreover, the low SNR of the individual spectra in the wavelength range of $\lambda \lesssim 3600$ Å does not allow for the direct one-to-one comparison between different individual exposures. As a result, an accurate understanding of the possible UVES systematics requires some other absolute references and/or spectra of bright objects. Asteroids are ideally suited for this kind of analysis (see Molaro et al. 2008) as they are very bright, their radial velocities are known to an accuracy of 1 m s^{-1}and their spectra are filled with the solar absorption features throughout any spectral range of interest. Several asteroids have been observed with UVES during different observing cycles for the purpose of tracking the possible wavelength calibration issues in UVES. In this section, we make use of the spectra of these objects observed with UVES to investigate the possible wavelength-dependent velocity shifts during different cycles. To do so, we select asteroids that were observed with UVES setting of 390 nm in the BLUE similar to our observations (see Table 1). Table 2 shows the observing log of the asteroids used in our analysis. We reduced these data following the same procedure described in Section 2 while using attached mode ThAr lamp for all the exposures. Table 2 shows that the time gap between different observations can vary from hours to years. This allows us to probe the UVES stability in both short and long terms. We further use the solar spectrum as an absolute reference and compare it with the UVES calibrated spectra of the asteroids.

3.2.1 Asteroid–asteroid comparison

We apply a cross-correlation analysis as described in Section 3.1 to compare asteroid spectra observed at different epochs. Fig. 5 shows the mean subtracted velocity shifts between the asteroids spectra observed with one or two nights of time gap during three

Table 2. Observing log of the UVES asteroids observations.

Name	Observation date	Exposure (s)	Seeing (arcsec)	Airmass	Spectral resolution	Slit width (arcsec)
IRIS	19-12-2006	300	1.21	1.50	815 92	0.6
	23-12-2006	300	1.48	1.47	822 15	0.6
	24-12-2006	300	1.25	1.46	815 23	0.6
	25-12-2006	300	1.35	1.44	813 81	0.6
	26-12-2006	450	1.79	1.44	814 79	0.6
	29-03-2012	600	1.07	1.14	591 07	0.8
	30-03-2012	600	1.20	1.17	591 51	0.8
	31-03-2012	600	1.19	1.18	584 39	0.8
	01-04-2012	600	0.99	1.21	585 38	0.8
CERES	31-10-2011	180	0.99	1.07	578 97	0.8
	31-10-2011	180	0.83	1.09	578 10	0.8
	01-11-2011	180	1.09	1.08	622 04	0.8
	30-10-2010	180	1.54	1.37	608 28	0.8
	01-11-2010	180	1.20	1.36	606 21	0.7
	03-11-2010	180	0.97	1.41	604 15	0.8
EROS	27-03-2012	600	1.14	1.12	588 52	0.8
	28-03-2012	600	1.23	1.18	585 35	0.8
	29-03-2012	600	1.72	1.22	588 41	0.8
	31-03-2012	600	0.97	1.19	576 81	0.8

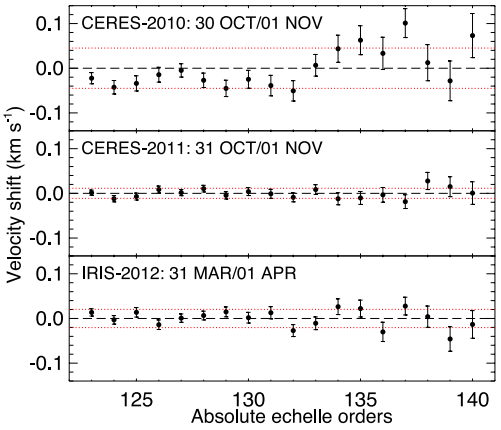

Figure 5. The velocity shifts between different asteroid exposures, after subtracting a mean velocity difference, with time gaps of one or two nights. The name of the asteroid and observing dates of the two exposures are shown in each panel. The standard deviation of the velocities are shown as dotted lines.

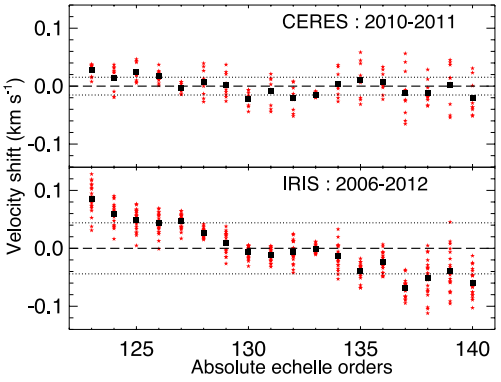

Figure 6. The velocity shifts measured in different echelle orders between asteroid exposures observed in different cycles. The dotted line shows the standard deviation of the velocity offsets.

different cycles. The abscissa is the absolute echelle order of the UVES and we have only shown the results for the orders that cover the wavelength range of 3330–3800 Å. The velocity offsets hardly reach a peak-to-peak difference of 50 m s^{-1} in the case of 2011 and 2012 observation. The scatter we notice here is very much similar to the one found by Molaro et al. (2008). The larger velocity errors and scatter seen in the case of 2010 observation is related to the lower SNR of the spectra of these asteroids as they are observed in a high airmass (see Table 2). However, this exercise shows that UVES is stable over short time-scales (i.e. a gap of up to 2 d). Fig. 6 shows the velocity offsets between the spectra of IRIS observed in 2006 and 2012 (bottom panel) and spectra of CERES observed in 2010 and 2011 (top panel). Asterisks are used to show the individual velocity offsets seen in each order and the filled squares show the mean of them. While in the case of CERES we find a (random) pattern (within a $\Delta v = 20\,\mathrm{m\,s^{-1}}$) similar to what we see in Fig. 5, in the case of IRIS there exists a clear steep increase of the mean velocity offsets as one goes towards lower echelle orders (or longer wavelengths). The wavelength-dependent velocity shifts seen in the case of IRIS is a signature of a severe systematic effect affecting the UVES spectrum taken in the year 2012 as suggested by our cross-correlation analysis of the quasar spectra (see Fig. 4). As the experiment carried out here is relative, we cannot clearly conclude whether the problem comes from either

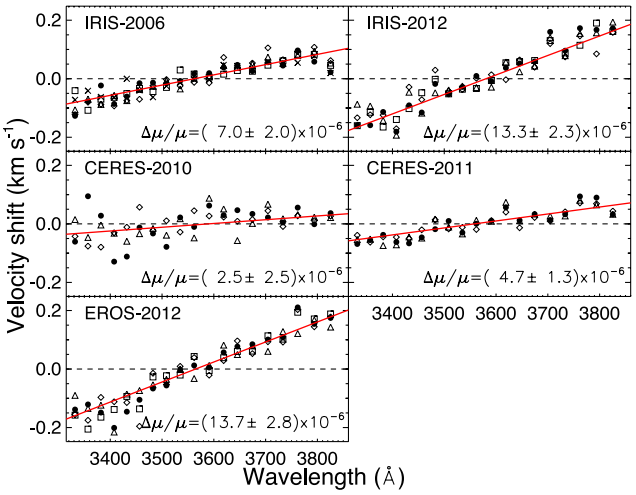

Figure 7. The velocity shift measurements using cross-correlation analysis between solar and asteroids spectra. The solid line in each panel shows the fitted line to the velocities. The $\Delta\mu/\mu$ corresponding to the slope of the fitted straight line is also given in each panel.

of the cycles or both. However, Molaro et al. (2008) did not find any wavelength-dependent systematics while comparing its absorption wavelengths in IRIS spectrum taken in the year 2006 with those of solar spectra for $\lambda \geq 4000$ Å. Unravelling this problem requires a very accurate absolute wavelength reference. We will consider the solar spectrum as an absolute reference for this purpose in the next section for further exploring this systematic.

3.2.2 *Solar–asteroid comparison*

Molaro et al. (2008) have used the very accurate wavelengths of the solar absorption lines in the literature as the absolute reference and compared them with the measured wavelengths of the same lines in the asteroid spectrum observed with UVES. Unfortunately, such an exercise is only possible for $\lambda \geq 4000$ Å as the solar absorption lines are severely blended for shorter wavelengths. However, using an accurately calibrated solar spectrum, we can cross-correlate it with the asteroid spectra of different years. We use the solar spectra discussed in Kurucz (2005, 2006) as the solar spectrum template.[2] This spectrum is corrected for telluric lines and the wavelength scale of the spectrum is corrected for the gravitational redshift ($\sim$0.63 km s^{-1}) and given in air. Therefore, we used UVES spectra before applying air-to-vacuum conversion for the correlation analysis. The uncertainties associated with the absolute wavelength scale of Kurucz (2005) is $\sim$100 m s^{-1}. We then measure the velocity offset between the solar and asteroid spectra in windows of the sizes of the UVES orders between 3330 and 3800 Å.

The results of the correlation analysis are presented in Fig. 7 as the solar–asteroid offset velocity versus the wavelength. Different symbols in each panel correspond to different asteroid exposures obtained within a period of couple of days. We have subtracted the mean velocity offset (coming from the radial velocity differences) in each case to bring the mean level to zero. A qualitative inspection shows that the velocity offsets in all cases increase as wavelengths increase though with different slopes for different years. Obviously, the two asteroids spectra acquired in 2012 show the largest slopes. As wavelength-dependent velocity shifts can mimic

[2] The spectrum is taken from http://kurucz.harvard.edu/sun/fluxatlas2005/.

a non-zero $\Delta\mu/\mu$, it is important to translate the observed trend to an apparent $\Delta\mu/\mu$. To estimate what is the effect of such a wavelength-dependent systematics in our $\Delta\mu/\mu$ measurements, we carried out the following exercise: (1) we fit a straight line to the velocity offset versus wavelength to get $\Delta v(\lambda)$, (2) finding the offset Δv and $\sigma_{\Delta v}$ at the observed wavelengths of our interested H_2 lines and assign a K_i to each Δv, (3) generating 2000 Gaussian realizations of each Δv (or reduced redshift) with the scatter of $\sigma_{\Delta v}$, (4) $\Delta\mu/\mu$ measurements from reduced redshift versus K analysis for each of the 500 realizations and (5) finding the mean and the scatter of the distribution as the systematic $\Delta\mu/\mu$ and its error. In Fig. 7, we have shown the estimated $\Delta\mu/\mu$ for each of the asteroid data. Typical error in $\Delta\mu/\mu$ is found to be 2.5×10^{-6}. The minimum $\Delta\mu/\mu = (2.5 \pm 2.5) \times 10^{-6}$ is obtained for the case of CERES-2010 observation. Spectra of IRIS-2012 and EROS-2012 show trends that are significant at more than 4.5σ level. These trends translates to a $\Delta\mu/\mu$ of $(13.3 \pm 2.3) \times 10^{-6}$ and $(13.7 \pm 2.8) \times 10^{-6}$, respectively, for IRIS-2012 and EROS-2012. This clearly confirms our finding that the UVES data acquired in 2012 have large wavelength drifts. As the amplitude of $\Delta\mu/\mu$ from the wavelength drift noted above is close to $\Delta\mu/\mu$ we wish to detect with our H_2 lines, it is important to remove these systematics from the data. Therefore, in what follows, in addition to standard $\Delta\mu/\mu$ measurements we also present $\Delta\mu/\mu$ measurements after correcting the redshifts of H_2 lines using the relationship found between the velocity offset and wavelength for the asteroid spectrum obtained closest to the quasar observations.

In summary, the analysis presented in this section suggests that one of the exposures (EXP19) shows a systematically large shift compared to the rest of the data. Therefore, we exclude this exposure when we discuss our final combined data to measure $\Delta\mu/\mu$. Our analysis also suggests the existence of wavelength-dependent velocity shift in particular in the spectra acquired in 2012. Therefore, we present our results for combined data of only first two cycles of data to gauge the influence of wavelength dependence drift in the data acquired in 2012.

4 CONSTRAINTS ON $\Delta\mu/\mu$

The $z = 2.4018$ DLA towards HE 0027−1836 produces more than 100 H_2 absorption lines in the observed wavelength range of 3330–3800 Å (see figs 19–25 in Noterdaeme et al. 2007). These are from different rotational states spanning from $J = 0$ to $J = 6$. While we detect a couple of transitions of $J = 6$ in absorption, they are too weak to lead to any reasonable estimation of the absorption line parameters (in particular the accurate value of z) of this level. Therefore, we do not make use of them for constraining $\Delta\mu/\mu$. For each rotational level, we detect several absorption lines arising from transitions having wide range of oscillator strengths. This makes it possible to have a very reliable estimation of fitting parameters and associated errors in our Voigt profile analysis of H_2 lines. From all the detected H_2 absorption, we select 71 useful lines for constraining $\Delta\mu/\mu$, out of which 24 may have a mild contamination in the wings from other unrelated absorption features. These mildly contaminated H_2 lines are also included in the analysis as their line centroids are well defined and the additional contaminations can be modelled accurately through multiple-component Voigt-profile fitting (see Fig. 9 and figures of Appendix C). H_2 lines used in the current study and results of the single component fit are presented in Table B1.

Noterdaeme et al. (2007) have found that the width of high J lines are systematically broader than that of low J lines when a single Voigt profile component was used. As our combined spectrum has a better SNR and pixel sampling compared to that used in Noterdaeme et al. (2007), we revisit the Voigt profile fitting, using VPFIT,[3] before measuring $\Delta\mu/\mu$. First, we fit all the identified H_2 transitions considering single b and z for all the levels and with the column density being different for different J-levels. Our best-fitting model has a reduced χ^2 of 1.421. The best-fitting value of the b-parameter is $2.10 \pm 0.04\,\mathrm{km\,s^{-1}}$. In addition, the derived column densities suggest an ortho-to-para ratio (OPR; see equation 1 of Srianand et al. 2005, for the definition) of 11.55 ± 1.42, while ≤ 3 is expected in a normal local thermal equilibrium (LTE) conditions. Next, we tried the fit very similar to that of Noterdaeme et al. (2007), where we have allowed the b-parameter to be different for different J-levels. In this case, the best fit is obtained with a reduced χ^2 of 1.190 and we notice that the OPR is 2.26 ± 0.15 as expected in the cold interstellar medium. Most of the total H_2 column density in this system is contributed by $J = 0$ and $J = 1$ levels. The best-fitting b-parameters are $0.89 \pm 0.05\,\mathrm{km\,s^{-1}}$ and $1.40 \pm 0.04\,\mathrm{km\,s^{-1}}$, respectively, for $J = 0$ and $J = 1$ levels. The abnormal values of OPR obtained when we fix b to be same for all J-levels can be attributed to the line saturation and the average b being much higher than the best-fitting b-values of $J = 0$ and $J = 1$. This exercise confirms the finding of Noterdaeme et al. (2007) that the absorption profile of high J-levels are broader than that of the low-J ones. This is one of the models we use in our analysis to find the best-fitting value of $\Delta\mu/\mu$. As pointed out by Noterdaeme et al. (2007), observed differences in the excitation temperatures and velocity width of high and low J-levels may point towards multiphase nature of the absorbing gas. In order to take this into account we allow for the mean redshift of absorption from different J-levels to be different in our analysis.

Alternatively, one could model the two-phase nature of the absorbing gas by using two-component Voigt profile fits. In this case, we constrain z and b of the two components to be the same for different J-levels and perform Voigt profile fits. Our best-fitting model has a reduced χ^2 of 1.192 with two components having $b = 0.94 \pm 0.04$ and $1.89 \pm 0.3\,\mathrm{km\,s^{-1}}$ and velocity separation of $4.4 \pm 0.2\,\mathrm{km\,s^{-1}}$. This reduced χ^2 is very similar to what we found for the single-component fit with different b-values for different J-levels discussed above. The first component at $z = 2.401\,842$ contains ∼99 per cent of the total H_2 column density and has an OPR of 2.27 ± 0.13. The second weaker component has an OPR of 3.07 ± 0.42. We further model the H_2 lines with two components while allowing different J-levels to have different b-values. In this model, z is constrained to be same for all J-levels. The best-fitting model in such a case has a reduced χ^2 of 1.177 with two components having a velocity separation of $4.0 \pm 0.4\,\mathrm{km\,s^{-1}}$. The reduced χ^2 is slightly improved in comparison with the case where b was tied. The first component at $z = 2.401\,844$ contains more than 99 per cent of the total H_2 column density and has an OPR of 2.11 ± 0.16. The second weaker component has an OPR of 2.92 ± 0.57. Unlike the previous two-component model, here both components have OPR consistent with what is expected under the LTE conditions. We consider this two-component model as the second case while measuring the $\Delta\mu/\mu$ value from our data.

There are two approaches used in literature to measure $\Delta\mu/\mu$ using H_2 absorption lines: (i) linear regression analysis of z_{red} versus K_i with $\Delta\mu/\mu$ as the slope (see for example Varshalovich & Levshakov 1993; Ivanchik et al. 2005; Reinhold et al. 2006; Wendt

[3] http://www.ast.cam.ac.uk/∼rfc/vpfit.html

Table 3. Results of the Voigt profile analysis for different J-levels in HE 0027−1836.

J-level	N	z	σ_z (km s^{-1})	δv (km s^{-1})	log[N(H$_2J$)] (log[cm^{-2}])	b (km s^{-1})
(1)	(2)	(3)	(4)	(5)	(6)	(7)
0	6	2.401 8452	0.07	0.00	16.91 ± 0.02	0.90 ± 0.06
1	14	2.401 8486	0.05	0.30	17.27 ± 0.02	1.41 ± 0.04
2	16	2.401 8499	0.07	0.41	14.95 ± 0.02	2.68 ± 0.07
3	12	2.401 8522	0.08	0.62	15.00 ± 0.02	3.34 ± 0.14
4	13	2.401 8513	0.11	0.54	14.19 ± 0.02	2.55 ± 0.38
5	10	2.401 8550	0.15	0.87	13.91 ± 0.02	3.89 ± 0.31

Column (1): indices for different rotational levels. Column (2): number of transitions in the given J-level. Column (3): mean weighted redshift of all transitions having same J-level. Column (4): redshift error in km s^{-1}. Column (5): redshift difference between the given J-level and $J = 0$ in km s^{-1}. Column (6): the log of the H_2 column density for different J-levels in cm^{-2}. Column (7): b parameter in km s^{-1} for different J-levels.

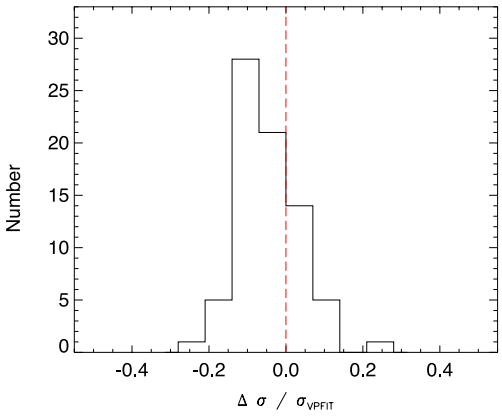

Figure 8. The distribution of the relative redshift error differences between VPFIT output and simulation. Here, $\Delta\sigma = \sigma_{\rm simulation} - \sigma_{\rm VPFIT}$. In 73 per cent of the simulated cases, the VPFIT error is larger than that of the simulation. This suggests that the statistical redshift errors from VPFIT are not underestimated.

& Molaro 2011) or (ii) use $\Delta\mu/\mu$ as an additional parameter in the VPFIT program (see for example King et al. 2008; Malec et al. 2010; King et al. 2011). We employ both the methods to derive $\Delta\mu/\mu$ from our data considering two cases: (i) single-component Voigt profile fit (called case-A) and (ii) two-component fit (called case-B).

4.1 Statistical errors from VPFIT

The VPFIT program estimates errors in each parameter only using the diagonal terms of the covariance matrix. These are reliable in cases where the lines are not strongly contaminated and are resolved out of the instrumental resolution. Measured b-parameters of the H_2 lines detected towards HE 0027−1836, especially those from $J = 0$ and $J = 1$ levels, are several times smaller than the instrumental resolution which is ∼5.0 km s^{-1} (see Table 3). In such cases, the reliability of the VPFIT errors should be investigated (see Carswell et al. 2011). To do so, we generate 100 simulated spectra with a same SNR as the final combined spectrum. For this, we consider our best-fitting single-component Voigt profile model obtained by VPFIT and add Gaussian noise to achieve the same SNR as the original spectrum. We then fit the H_2 lines of each mock spectrum using the same fitting regions and initial guess parameters as those used in the case of our best-fitting model. Finally, for each of the H_2 transitions we compare the 1σ distribution from the 100 mock redshifts with the estimated error from VPFIT. Fig. 8 shows the distribution of the relative error differences of redshifts, (i.e. $(\sigma_{\rm simulation} - \sigma_{\rm VPFIT})/\sigma_{\rm VPFIT}$) of all the H_2 lines used in this analysis. Clearly, when we use majority of the transitions, VPFIT does not underestimate the redshift errors. As it can be seen from this histogram, the two errors are always consistent and in ∼73 per cent of cases VPFIT predicts a higher value for the error. We confirm that the same result holds for errors associated with N- and b-parameters obtained from the VPFIT. We repeated the analysis for the two-component fit as well and found that the error obtained from the VPFIT adequately represents the statistical error of the parameters. Therefore, we will only use the VPFIT errors as statistical errors in redshifts.

4.2 $\Delta\mu/\mu$ measurements using z-versus K analysis

Following previous studies (Ivanchik et al. 2005; Reinhold et al. 2006; Ubachs et al. 2007; Wendt & Molaro 2011, 2012), we carry out $\Delta\mu/\mu$ measurements based on the z-versus K linear regression analysis in this section. We use the redshifts of individual transitions obtained from the VPFIT for case-A discussed above. Fig. C1 shows our best-fitting Voigt profile for $J = 3$ transitions for the combined spectrum made of all exposures excluding EXP19. H_2 transitions L1P3, L2P3, L4P3, L5R3, W0Q3 and L10P3 are the examples of what we classify as CLEAN lines. The rest of the H_2 absorption lines shown in Fig. C1 are classified as blended. Voigt profile fits to these lines are performed by suitably taking care of the blending. Fits to H_2 lines from other J-levels are shown in Appendix C. The fitting results for H_2 lines used in $\Delta\mu/\mu$ measurements are presented in Appendix B. Table 3 summarizes the H_2 column density, b-parameter and the mean redshift for each J-level. As J-level increases, the velocity offset with respect to $J = 0$ and the b-parameter of the corresponding level also increases. The only exception is $J = 4$ that its velocity offset and b-parameter are less than those of $J = 3$ but still larger than $J = 2$.

In our linear regression analysis, we do not use the redshift errors from VPFIT as our analysis in Section 3.2 shows that the wavelengths of different regions may be affected by some systematic error. As this error is independent of the statistical redshift error, it makes the distribution of the H_2 redshift to have a larger scatter than that allowed by the statistical error we get from the Voigt profile fitting. Therefore, we use a bootstrap technique for estimating the realistic error of our regression analysis. To do so, we generate 2000 random realizations of the measured redshifts and estimate $\Delta\mu/\mu$ for each of these realizations. We finally quote the 1σ scatter of the 2000 $\Delta\mu/\mu$ as the estimated error in $\Delta\mu/\mu$. From Table 3, we can see that the mean redshifts of different J-levels may be different in this case. Therefore, in our analysis, we allow for the redshifts of different J-levels to be different by allowing the intercept in z versus K plot to be different for different J-levels.

In Fig. 10, we plot the reduced redshift versus K for different transitions. The points from different J-levels are marked with different symbols. The best-fitting lines for points from different J-levels are also shown in the figure with different line styles. As discussed before, we constrained the slope (i.e. $\Delta\mu/\mu$) of these lines to be same while allowing for the intercept (i.e. mean redshift) to be different for different J-levels. The best-fitting value for $\Delta\mu/\mu$ is 20.0 ± 9.3 ppm (see column 2 of the last row in Table 4). The quoted error is obtained using bootstrapping as discussed above.

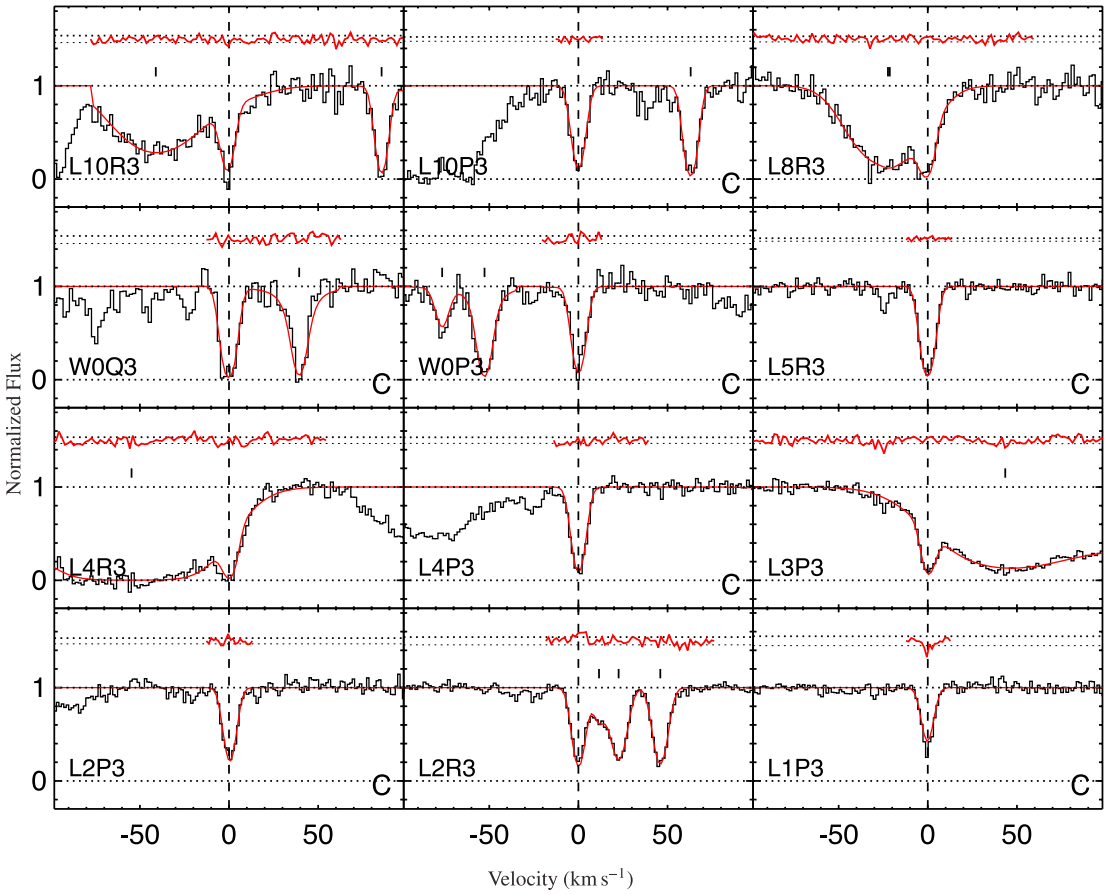

Figure 9. Absorption profile of H_2 transitions of $J = 3$ level and the best-fitting Voigt profile to the combined spectrum of all exposures after excluding EXP19. The normalized residual (i.e. ([data]−[model])/[error]) for each fit is also shown in the top of each panel along with the 1σ line. We identify the clean absorption lines by using the letter 'C' in the right bottom of these transitions. The vertical ticks mark the positions of fitted contamination.

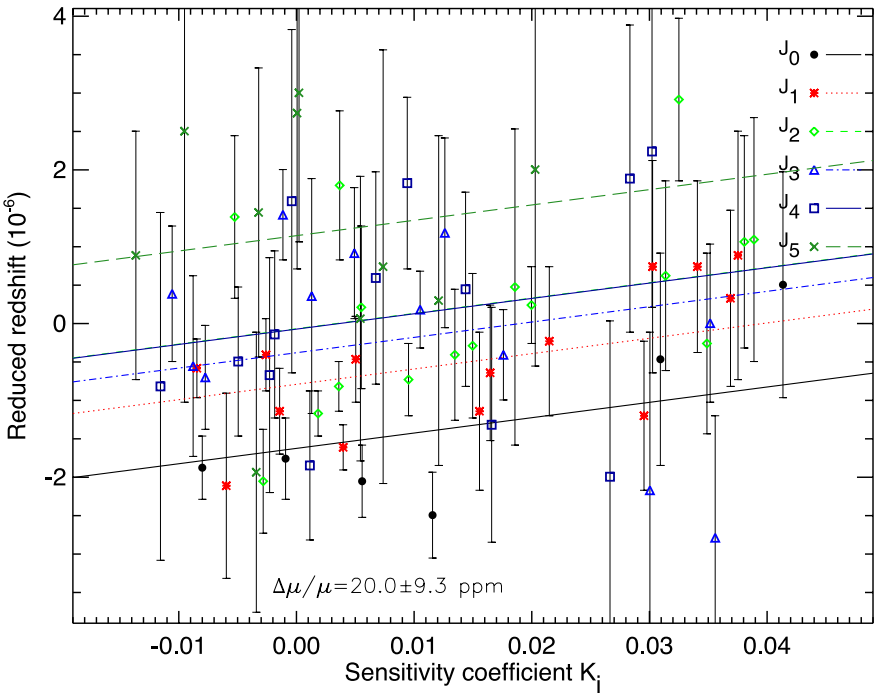

Figure 10. Reduced redshift versus the K_i for all the fitted H_2 lines in the case of combined spectrum of all exposures except EXP19. Lines from different J-levels are plotted with different symbols. The best-fitting linear line for different J-levels with the constraint that the slope should be same is also shown.

Table 4. $\Delta\mu/\mu$ measurement for each cycle in 10^{-6} unit.

	z versus K		VPFIT									
	1-component		1-component					2-components				
(1)	(2)	(3)	(4)	(5)	(6)	(7)	(8)	(9)	(10)	(11)	(12)	(13)
Cycle	Original	Corrected[b]	Original	χ^2_ν	AICC	Corrected[b]	χ^2_ν	Original	χ^2_ν	AICC	Corrected[b]	χ^2_ν
1	-1.7 ± 16.3	-4.6 ± 16.8	$+21.1 \pm 10.0$	1.037	6302	$+19.8 \pm 9.9$	1.029	-11.7 ± 12.2	1.032	6295	-12.1 ± 11.8	1.022
2	$+30.2 \pm 12.2$	$+26.7 \pm 12.7$	$+15.5 \pm 10.5$	0.974	5948	$+10.0 \pm 10.5$	0.972	$+10.7 \pm 11.9$	0.969	5936	$+5.2 \pm 11.9$	0.967
3[a]	$+41.6 \pm 19.5$	$+30.1 \pm 19.0$	$+30.2 \pm 14.3$	0.932	5705	$+14.5 \pm 12.5$	0.927	$+12.9 \pm 13.5$	0.912	5614	-0.8 ± 13.4	0.907
1+2	$+10.7 \pm 11.4$	$+13.8 \pm 10.2$	$+18.8 \pm 7.7$	1.128	6825	$+15.8 \pm 7.7$	1.123	$+0.8 \pm 8.6$	1.120	6794	-1.5 ± 8.7	1.115
1+2+3[a]	$+20.0 \pm 9.3$	$+15.0 \pm 9.3$	$+21.8 \pm 6.9$	1.188	7167	$+15.6 \pm 6.9$	1.179	-2.5 ± 8.1	1.178	7115	-7.6 ± 8.1	1.171

[a] Results of the cases in which EXP19 is excluded.
[b] Results after correcting the systematics based on the solar-asteroid cross-correlation.

As the wavelength-dependent velocity shift is found to be minimum in the case of first two cycles, we measured the $\Delta\mu/\mu$ using only the data obtained in the first two cycles (i.e. 13 exposures and total integration time of ∼23 h). We call this sub-sample as '1+2'. The results of the $\Delta\mu/\mu$ measurement for this case is also given in Table 4. We find $\Delta\mu/\mu = +10.7 \pm 11.4$ ppm. As expected, the mean $\Delta\mu/\mu$ obtained from this sub-sample is less than the one obtained for the whole sample. The amount of observing time in different cycles are, respectively, 10.4, 12.5 and 10.4 h for the first, second and third cycle. Therefore, we also measured $\Delta\mu/\mu$ using data obtained in individual cycles. The total observing time in each cycle is sufficiently good for estimating $\Delta\mu/\mu$ based on each cycle. We get $\Delta\mu/\mu = -1.7 \pm 16.3, +30.2 \pm 12.2$ and $+41.6 \pm 19.5$ ppm, respectively, for the first, second and third cycles. The progressive increase in the mean $\Delta\mu/\mu$ is consistent with what we notice in Fig. 7 for the asteroids.

The final combined spectrum used here is based on 18 exposures. With such a large number of exposures, in principle, the result of our analysis should not be sensitive to individual exposures. To test this we make 100 combined spectra of 15 randomly chosen individual exposures and measure $\Delta\mu/\mu$ using z versus K analysis of single-component fit (case-A) as discussed above for the full sample. Fig. 11 shows the distribution of the measured $\Delta\mu/\mu$. The mean we measure (i.e. 19.7×10^{-6}) is consistent with the mean we get for the full sample. The 1σ scatter around the mean is 3.6×10^{-6}. As expected, this is much smaller than the statistical error in individual measurements. Thus, we feel that the bootstrap method adequately quantifies the errors in our $\Delta\mu/\mu$ measurements.

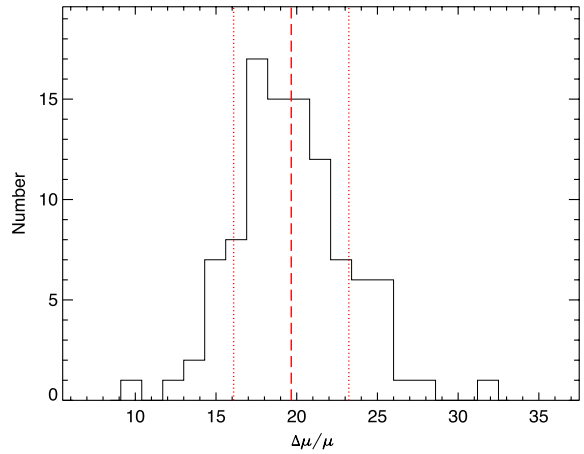

Figure 11. The distribution of 100 $\Delta\mu/\mu$ measured from combined spectra made out of 15 randomly chosen exposures. The long dashed and short dashed lines show the mean and 1σ scatter of the distribution which, respectively, are 19.7×10^{-6} and 3.6×10^{-6}.

Now, we will apply corrections to the velocity drift seen in the case of asteroids to the individual spectrum and see its effect in the $\Delta\mu/\mu$ measurements. To do so, we first shift the observed wavelength of each pixel of each individual exposure based on the modelled velocity offsets obtained from the solar–asteroid cross-correlation analysis in the corresponding observing cycle. We then combine these shifted individual spectra to make the final combined spectrum. Only in cycle-2 we have asteroid observations taken on the same nights of the quasar observation. In the other two cycles, the nearest asteroid observations are obtained within 3.5 months of the quasar observations. While this is not the ideal situation, this is the best we can do. Results of $\Delta\mu/\mu$ measurements after applying the drift correction for different cases are summarized in column 3 of Table 4. The results of $\Delta\mu/\mu$ before applying drift corrections are summarized in column 4 of Table 4. We find $\Delta\mu/\mu = +15.0 \pm 9.3$ ppm for the combined data after applying corrections. Clearly an offset at the level of 5 ppm comes from this effect alone in the combined data. We wish to note that the estimated $\Delta\mu/\mu$ after applying corrections should be considered as an indicative value as we do not have asteroid observations on the same nights of quasar observations. In addition, the quasar and asteroid observations are very different in terms of the exposure times and the source angular size.

We notice that because of severe blending, z versus K method cannot be easily applied to the two-component fit (case-B). In the following section, we obtain $\Delta\mu/\mu$ directly from VPFIT for both single- and two-component fits.

4.3 $\Delta\mu/\mu$ measurements using VPFIT

We performed the Voigt profile fitting of all the chosen H_2 lines keeping $\Delta\mu/\mu$ as an additional fitting parameter. The results are also summarized in columns 4–13 in Table 4. When we consider the single-component fit (case-A), we find $\Delta\mu/\mu = +21.8 \pm 6.9$ ppm for the full sample with a reduced χ^2 of 1.188 (see columns 4 and 5 in Table 4). This is very much consistent with what we have found above using z versus K analysis. We find the final $\Delta\mu/\mu$ value to be robust using different input parameter sets. When we fit the data obtained from first two cycles, we find $\Delta\mu/\mu = +18.8 \pm 7.7$ ppm with a reduced χ^2 of 1.128. This also confirms our finding that the addition of third year data increases the measured mean of $\Delta\mu/\mu$. Table 4 also summarizes the results of $\Delta\mu/\mu$ measurements for data taken on individual cycles. When we use the corrected spectrum for the full sample, we get $\Delta\mu/\mu = +15.6 \pm 6.9$ ppm. The $\Delta\mu/\mu$ measurements for different cases after applying the

correction and the corresponding reduced χ^2 are given in columns 7 and 8, respectively. As noted earlier the statistical errors from the VPFIT are about 25–30 per cent underestimated compared to the bootstrap errors obtained in the z versus K analysis. It is also clear from the table that correcting the velocity offset leads to the reduction of the $\Delta\mu/\mu$ up to 6.2 ppm for the combined data set. Column 6 in Table 4 gives the Akaike information criteria (AIC; Akaike 1974) corrected for the finite sample size (AICC; Sugiura 1978) as given in the equation 4 of King et al. (2011). We can use AICC in addition to the reduced χ^2 to discriminate between the models.

Next, we consider the two-component Voigt profile fits (i.e. case-B) where we keep $\Delta\mu/\mu$ as an additional fitting parameter. The results are also summarized in columns 9–13 of Table 4. The $\Delta\mu/\mu$ measurements, associated reduced χ^2 and AICC parameters for uncorrected data are given in columns 9, 10 and 11, respectively. Results for the corrected data are provided in columns 12 and 13. For the whole sample, we find $\Delta\mu/\mu = -2.5 \pm 8.1$ ppm with a reduced χ^2 of 1.177. The reduced χ^2 in this case is slightly lower than the corresponding single-component fit. In addition, we find that the difference in AICC is 52 in favour of two-component fit (i.e. case-B). Table 4 also presents results for individual cycle data for the two-component fit.

The comparison of AICC given in columns 6 and 11 of the Table 4 also clearly favours the two-component fit (i.e. case-B). Therefore, we will only consider measurements based on two-component fit in the following discussions. However, bootstrapping errors in the case of z versus K linear regression analysis (of single-component fit) are larger and robust when comparing with the errors from VPFIT. In the case of combined spectrum of all exposures (last row of Table 4) we need to quadratically add 6.2 ppm to the VPFIT error to get the z versus K error. This can be considered as typical contribution of the systematic errors. So we consider the two-component fit results with the enhanced error in further discussions.

5 DISCUSSION

We have analysed the H_2 absorption lines from a DLA at $z_{abs} = 2.4018$ towards HE 0027−1836 observed with VLT/UVES as part of the ESO Large Programme 'The UVES large programme for testing fundamental physics'. We carried out $\Delta\mu/\mu$ measurements based on z versus K analysis. Our cross-correlation analysis shows that one of the exposures has a large velocity shift with respect to the remaining exposures. Excluding this exposure from the combined spectrum we find a $\Delta\mu/\mu = (-2.5 \pm 8.1_{stat} \pm 6.2_{sys}) \times 10^{-6}$.

To understand the possible systematics affecting our observations, we studied the asteroids observed with VLT/UVES in different cycles. Comparing the asteroids spectra and very accurate solar spectrum, we show the existence of a wavelength-dependent velocity shift with varying magnitude in different cycles. Correcting our observations for these systematics, we measure $\Delta\mu/\mu = (-7.6 \pm 8.1_{stat} \pm 6.2_{sys}) \times 10^{-6}$. Our measurement is consistent with no variation in μ over the last 10.8 Gyr at a level of one part in 10^5. Our null result is consistent with $\Delta\mu/\mu$ measurements in literature from analysis of different H_2-bearing sightlines (Thompson et al. 2009b, table 1).

Fig. 12 summarizes the $\Delta\mu/\mu$ measurements based on different approaches at different redshifts. As can be seen our new measurement is also consistent with the more recent accurate measurements using H_2 at $z \geq 2$. Wendt & Molaro (2012) found a $\Delta\mu/\mu = (4.3 \pm 7.2) \times 10^{-6}$ using the H_2 absorber

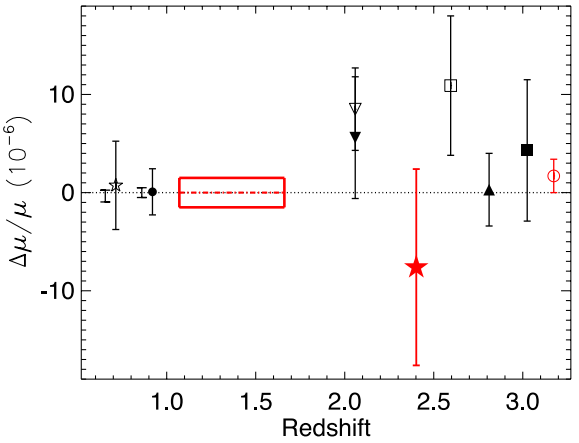

Figure 12. Comparing $\Delta\mu/\mu$ measurement in this work and those in the literature. All measurements at $2.0 < z < 3.1$ are based on the analysis of H_2 absorption. The filled asterisk shows our result. The downward empty and filled triangles are the $\Delta\mu/\mu$ measurements from van Weerdenburg et al. (2011) and Malec et al. (2010), respectively. The filled upward triangle and the empty and filled squares are, respectively, from King et al. (2011), King et al. (2008) and Wendt & Molaro (2012). The solid box and the open circle present the constraint obtained, respectively, by Rahmani et al. (2012) and Srianand et al. (2010) based on the comparison between 21-cm and metal lines in Mg II absorbers under the assumption that α and g_p have not varied. The $\Delta\mu/\mu$ at $z < 1$ are based on ammonia and methanol inversion transitions and their 5σ errors are shown. The two measurements at $z \sim 0.89$ with larger and smaller errors are, respectively, from Henkel et al. (2009) and Bagdonaite et al. (2013) based on the same system. The two $\Delta\mu/\mu$ at $z \sim 0.684$ with larger and smaller errors are, respectively, from Murphy et al. (2008) and Kanekar (2011) based on the same system.

at $z = 3.025$ towards Q0347−383. King et al. (2011) and van Weerdenburg et al. (2011) used H_2 and HD absorbers at, respectively, $z = 2.811$ and 2.059 towards Q0528−250 and J2123−005 to find $\Delta\mu/\mu = (0.3 \pm 3.2_{stat} \pm 1.9_{sys}) \times 10^{-6}$ and $(8.5 \pm 4.2) \times 10^{-6}$. The measurement towards Q0528−250 is the most stringent $\Delta\mu/\mu$ measurement reported till date. However, large discrepancies (a factor of ∼50) in the reported $N(H_2)$ values by King et al. (2011) and Noterdaeme et al. (2008) are a concern and their effect on $\Delta\mu/\mu$ needs to be investigated. King et al. (2008) have found $\Delta\mu/\mu = (10.9 \pm 7.1) \times 10^{-6}$ at $z = 2.595$ towards Q0405−443. Using these measurements and ours, we find the weighted mean of $\Delta\mu/\mu = (4.1 \pm 3.3) \times 10^{-6}$. If we use the measurement of Thompson et al. (2009b) of $\Delta\mu/\mu = (3.7 \pm 14) \times 10^{-6}$ for the system towards Q0405−443, we get the mean value of $\Delta\mu/\mu = (3.2 \pm 2.7) \times 10^{-6}$. However, we wish to point out that three out of four UVES-based measurements show positive values of $\Delta\mu/\mu$. As any wavelength-dependent drift in these cases could bias these measurements towards positive $\Delta\mu/\mu$ (see Section 3.2.2), we should exercise caution in quoting combined $\Delta\mu/\mu$ measurements.

Best constraints on $\Delta\mu/\mu$ in quasar spectra are obtained using either NH_3 or CH_3OH (Murphy et al. 2008; Henkel et al. 2009; Kanekar 2011; Bagdonaite et al. 2013). These measurements reach a sensitivity of 10^{-7} in $\Delta\mu/\mu$. However, only two systems at high redshift are used for these measurements and both at $z < 1$. Based on 21-cm absorption, we have $\Delta\mu/\mu = (0.0 \pm 1.5) \times 10^{-6}$ (at $z \sim 1.3$ by Rahmani et al. 2012) and $\Delta\mu/\mu = (-1.7 \pm 1.7) \times 10^{-6}$ (at $z \sim 3.2$ by Srianand et al. 2010). While these measurements are more stringent than H_2-based measurements, one has to assume no

variation in α and g_p to get a constraint on $\Delta\mu/\mu$. Also care needs to be taken to minimize the systematics related to the line of sight to radio and optical emission being different.

ACKNOWLEDGEMENTS

RS and PPJ gratefully acknowledge support from the Indo-French Centre for the Promotion of Advanced Research (Centre Franco-Indian pour la Promotion de la Recherche Avancée) under contract No. 4304-2. PM and CJM acknowledge the financial support of grant PTDC/FIS/111725/2009 from FCT (Portugal). CJM is also supported by an FCT Research Professorship, contract reference IF/00064/2012. The work of SAL is supported by DFG Sonderforschungsbereich SFB 676 Teilprojekt C4. MTM thanks the Australian Research Council for *Discovery Project* grant DP110100866 which supported this work.

REFERENCES

Agafonova I. I., Molaro P., Levshakov S. A., Hou J. L., 2011, A&A, 529, A28
Agafonova I. I., Levshakov S. A., Reimers D., Hagen H.-J., Tytler D., 2013, A&A, 552, A83
Akaike A., 1974, IEEE Trans. Autom. Control, 19, 716
Amendola L., Leite A. C. O., Martins C. J. A. P., Nunes N. J., Pedrosa P. O. J., Seganti A., 2012, Phys. Rev. D, 86, 063515
Bagdonaite J., Jansen P., Henkel C., Bethlem H. L., Menten K. M., Ubachs W., 2013, Sci, 339, 46
Bailly D., Salumbides E. J., Vervloet M., Ubachs W., 2010, Mol. Phys., 108, 827
Carswell R. F., Jorgenson R. A., Wolfe A. M., Murphy M. T., 2011, MNRAS, 411, 2319
Chand H., Srianand R., Petitjean P., Aracil B., Quast R., Reimers D., 2006, A&A, 451, 45
Cowie L. L., Songaila A., 1995, ApJ, 453, 596
D'Odorico S., Cristiani S., Dekker H., Hill V., Kaufer A., Kim T., Primas F., 2000, in Bergeron J., ed., Proc. SPIE Conf. Ser. Vol. 4005, Discoveries and Research Prospects from 8- to 10-Meter-Class Telescopes. SPIE, Bellingham, p. 121
Dekker H., D'Odorico S., Kaufer A., Delabre B., Kotzlowski H., 2000, in Iye M., Moorwood A. F., eds, Proc. SPIE Conf. Ser. Vol. 4008, Optical and IR Telescope Instrumentation and Detectors. SPIE, Bellingham, p. 534
Edlén B., 1966, Metrologia, 2, 71
Ferreira M. C., Julião M. D., Martins C. J. A. P., Monteiro A. M. R. V. L., 2012, Phys. Rev. D, 86, 125025
Henkel C. et al., 2009, A&A, 500, 725
Ivanchik A., Petitjean P., Varshalovich D., Aracil B., Srianand R., Chand H., Ledoux C., Boissé P., 2005, A&A, 440, 45
Jorgenson R. A., Murphy M. T., Thompson R., Carswell R. F., 2013, MNRAS, preprint (arXiv:1307.4429)
Kanekar N., 2011, ApJ, 728, L12
King J. A., Webb J. K., Murphy M. T., Carswell R. F., 2008, Phys. Rev. Lett., 101, 251304
King J. A., Murphy M. T., Ubachs W., Webb J. K., 2011, MNRAS, 417, 3010
Kozlov M. G., Levshakov S. A., 2013, Annalen der Physik, 525, 452
Kurucz R. L., 2005, Mem. Soc. Astron. Ital., 8, 189
Kurucz R. L., 2006, preprint (astro-ph/0605029)
Ledoux C., Petitjean P., Srianand R., 2003, MNRAS, 346, 209
Levshakov S. A., Dessauges-Zavadsky M., D'Odorico S., Molaro P., 2002, MNRAS, 333, 373
Levshakov S. A., Centurión M., Molaro P., D'Odorico S., Reimers D., Quast R., Pollmann M., 2006, A&A, 449, 879
Levshakov S. A., Combes F., Boone F., Agafonova I. I., Reimers D., Kozlov M. G., 2012, A&A, 540, L9
MacAlpine G. M., Feldman F. R., 1982, ApJ, 261, 412
Malec A. L. et al., 2010, MNRAS, 403, 1541
Molaro P., Levshakov S. A., Monai S., Centurión M., Bonifacio P., D'Odorico S., Monaco L., 2008, A&A, 481, 559
Molaro P. et al., 2013, A&A, 555, A68
Murphy M. T., Flambaum V. V., Muller S., Henkel C., 2008, Sci, 320, 1611
Noterdaeme P., Ledoux C., Petitjean P., Le Petit F., Srianand R., Smette A., 2007, A&A, 474, 393
Noterdaeme P., Ledoux C., Petitjean P., Srianand R., 2008, A&A, 481, 327
Olive K., Skillman E., 2004, ApJ, 617, 29
Petitjean P., Srianand R., Ledoux C., 2000, A&A, 364, L26
Petitjean P., Srianand R., Chand H., Ivanchik A., Noterdaeme P., Gupta N., 2009, Space Sci. Rev., 35
Petrov Y., Nazarov A., Onegin M., Petrov V., Sakhnovsky E., 2006, Phys. Rev. C, 74
Rahmani H., Srianand R., Gupta N., Petitjean P., Noterdaeme P., Vásquez D. A., 2012, MNRAS, 425, 556
Reinhold E., Buning R., Hollenstein U., Ivanchik A., Petitjean P., Ubachs W., 2006, Phys. Rev. Lett., 96, 151101
Rosenband T. et al., 2008, Sci, 319, 1808
Shelkovnikov A., Butcher R. J., Chardonnet C., Amy-Klein A., 2008, Phys. Rev. Lett., 100, 150801
Srianand R., Petitjean P., Ledoux C., Ferland G., Shaw G., 2005, MNRAS, 362, 549
Srianand R., Gupta N., Petitjean P., Noterdaeme P., Ledoux C., 2010, MNRAS, 405, 1888
Srianand R., Gupta N., Petitjean P., Noterdaeme P., Ledoux C., Salter C. J., Saikia D. J., 2012, MNRAS, 421, 651
Sugiura N., 1978, Commun. Stat. A - Theory Methods, 7, 13
Thompson R. I., 1975, Astrophys. Lett., 16, 3
Thompson R. I., Bechtold J., Black J. H., Martins C. J. A. P., 2009a, New Astron., 14, 379
Thompson R. I. et al., 2009b, ApJ, 703, 1648
Tzanavaris P., Murphy M. T., Webb J. K., Flambaum V. V., Curran S. J., 2007, MNRAS, 374, 634
Ubachs W., Buning R., Eikema K. S. E., Reinhold E., 2007, J. Mol. Spectrosc., 241, 155
Uzan J.-P., 2011, Living Rev. Relativ., 14, 2
van Weerdenburg F., Murphy M. T., Malec A. L., Kaper L., Ubachs W., 2011, Phys. Rev. Lett., 106, 180802
Varshalovich D. A., Levshakov S. A., 1993, Sov. J. Exp. Theor. Phys. Lett., 58, 237
Wendt M., Molaro P., 2011, A&A, 526, A96
Wendt M., Molaro P., 2012, A&A, 541, A69
Whitmore J. B., Murphy M. T., Griest K., 2010, ApJ, 723, 89

APPENDIX A: RESULTS OF CORRELATION ANALYSIS

Table A1. Measured shifts between the 6 individual exposures of HE 0027−1836 observed in 2010 and the combined exposure made out of all 19 exposures.

Regions	EXP01 ($km\,s^{-1}$)	EXP02 ($km\,s^{-1}$)	EXP03 ($km\,s^{-1}$)	EXP04 ($km\,s^{-1}$)	EXP05 ($km\,s^{-1}$)	EXP06 ($km\,s^{-1}$)
3319−3345	+0.13 ± 0.20	+0.16 ± 0.18	+0.00 ± 0.09	−0.06 ± 0.12	+0.05 ± 0.12	+0.16 ± 0.19
3345−3370	+0.05 ± 0.15	−0.01 ± 0.13	+0.06 ± 0.07	−0.05 ± 0.13	+0.05 ± 0.12	+0.05 ± 0.16
3370−3395	−0.13 ± 0.17	+0.19 ± 0.15	+0.00 ± 0.07	+0.06 ± 0.12	+0.01 ± 0.11	−0.02 ± 0.16
3395−3421	−0.04 ± 0.15	−0.11 ± 0.15	+0.02 ± 0.07	+0.07 ± 0.15	+0.02 ± 0.11	−0.25 ± 0.16
3421−3446	+0.10 ± 0.15	−0.07 ± 0.16	−0.03 ± 0.07	+0.01 ± 0.13	−0.06 ± 0.10	+0.02 ± 0.17
3446−3472	+0.13 ± 0.14	−0.10 ± 0.17	+0.02 ± 0.08	+0.00 ± 0.15	+0.02 ± 0.10	+0.06 ± 0.19
3498−3523	−0.02 ± 0.16	+0.20 ± 0.16	+0.06 ± 0.10	+0.10 ± 0.15	−0.11 ± 0.11	−0.18 ± 0.17
3523−3552	−0.18 ± 0.12	−0.04 ± 0.15	+0.08 ± 0.09	−0.24 ± 0.12	−0.12 ± 0.10	−0.06 ± 0.14
3552−3578	+0.02 ± 0.14	−0.28 ± 0.16	+0.01 ± 0.08	+0.15 ± 0.14	−0.11 ± 0.12	+0.17 ± 0.19
3578−3607	−0.09 ± 0.14	−0.07 ± 0.13	+0.01 ± 0.07	−0.20 ± 0.15	+0.04 ± 0.10	+0.08 ± 0.17
3607−3636	−0.09 ± 0.12	−0.14 ± 0.14	+0.05 ± 0.08	−0.12 ± 0.11	−0.20 ± 0.09	+0.00 ± 0.13
3636−3662	−0.19 ± 0.15	−0.04 ± 0.15	−0.05 ± 0.10	+0.03 ± 0.16	−0.09 ± 0.13	+0.15 ± 0.17
3662−3691	−0.11 ± 0.10	+0.01 ± 0.10	+0.12 ± 0.06	−0.04 ± 0.09	−0.16 ± 0.08	+0.18 ± 0.12
3691−3719	−0.09 ± 0.13	−0.02 ± 0.15	+0.10 ± 0.09	−0.14 ± 0.13	−0.12 ± 0.10	+0.22 ± 0.15
3719−3750	+0.14 ± 0.13	−0.09 ± 0.14	+0.06 ± 0.08	−0.37 ± 0.14	−0.01 ± 0.10	−0.05 ± 0.15
3750−3780	+0.06 ± 0.14	+0.10 ± 0.12	+0.03 ± 0.08	−0.02 ± 0.12	−0.19 ± 0.09	+0.09 ± 0.16
Weighted mean and error	−0.03 ± 0.03	−0.02 ± 0.04	+0.03 ± 0.02	−0.06 ± 0.03	−0.07 ± 0.03	+0.04 ± 0.04
Weighted mean and error of six exposures			−0.01 ± 0.01			

Table A2. Measured shifts between the 7 individual exposures of HE 0027−1836 observed in 2011 and the combined exposure made out of all 19 exposures.

Regions	EXP07 ($km\,s^{-1}$)	EXP08 ($km\,s^{-1}$)	EXP09 ($km\,s^{-1}$)	EXP10 ($km\,s^{-1}$)	EXP11 ($km\,s^{-1}$)	EXP12 ($km\,s^{-1}$)	EXP13 ($km\,s^{-1}$)
3319−3345	+0.03 ± 0.15	+0.12 ± 0.20	−0.12 ± 0.15	−0.12 ± 0.18	+0.13 ± 0.14	−0.14 ± 0.13	+0.15 ± 0.14
3345−3370	+0.00 ± 0.12	+0.04 ± 0.17	−0.11 ± 0.14	+0.18 ± 0.15	+0.08 ± 0.13	−0.19 ± 0.13	+0.07 ± 0.12
3370−3395	−0.26 ± 0.14	−0.06 ± 0.17	+0.01 ± 0.13	+0.06 ± 0.14	+0.08 ± 0.14	+0.18 ± 0.14	+0.14 ± 0.13
3395−3421	+0.03 ± 0.14	−0.05 ± 0.16	−0.04 ± 0.16	−0.16 ± 0.16	−0.04 ± 0.14	+0.25 ± 0.13	−0.02 ± 0.12
3421−3446	+0.07 ± 0.16	+0.13 ± 0.16	−0.17 ± 0.14	−0.19 ± 0.13	+0.11 ± 0.13	+0.13 ± 0.14	+0.03 ± 0.15
3446−3472	+0.07 ± 0.14	+0.02 ± 0.18	−0.14 ± 0.14	+0.15 ± 0.13	−0.11 ± 0.13	+0.09 ± 0.15	−0.18 ± 0.16
3498−3523	−0.21 ± 0.14	+0.00 ± 0.18	+0.01 ± 0.13	+0.01 ± 0.16	−0.17 ± 0.15	−0.09 ± 0.16	−0.10 ± 0.16
3523−3552	+0.13 ± 0.13	+0.02 ± 0.15	+0.08 ± 0.11	−0.01 ± 0.14	−0.06 ± 0.13	+0.04 ± 0.14	−0.14 ± 0.12
3552−3578	+0.10 ± 0.14	−0.04 ± 0.18	+0.13 ± 0.13	−0.07 ± 0.13	+0.16 ± 0.14	−0.26 ± 0.17	−0.17 ± 0.14
3578−3607	+0.25 ± 0.15	−0.09 ± 0.15	−0.24 ± 0.13	+0.16 ± 0.13	−0.01 ± 0.13	+0.06 ± 0.15	−0.08 ± 0.14
3607−3636	+0.20 ± 0.13	+0.09 ± 0.14	+0.06 ± 0.12	−0.06 ± 0.13	−0.01 ± 0.13	−0.10 ± 0.13	−0.06 ± 0.11
3636−3662	−0.06 ± 0.15	−0.03 ± 0.14	+0.01 ± 0.13	−0.11 ± 0.16	+0.14 ± 0.14	+0.06 ± 0.17	−0.05 ± 0.15
3662−3691	−0.05 ± 0.09	−0.09 ± 0.09	−0.08 ± 0.09	−0.29 ± 0.10	−0.09 ± 0.09	+0.11 ± 0.10	−0.13 ± 0.10
3691−3719	−0.03 ± 0.14	+0.21 ± 0.14	−0.09 ± 0.12	−0.02 ± 0.13	−0.03 ± 0.12	+0.03 ± 0.13	−0.11 ± 0.13
3719−3750	−0.04 ± 0.13	−0.11 ± 0.14	−0.22 ± 0.15	−0.25 ± 0.14	−0.02 ± 0.13	+0.00 ± 0.14	+0.14 ± 0.13
3750−3780	−0.26 ± 0.14	+0.06 ± 0.13	−0.03 ± 0.13	−0.07 ± 0.15	+0.16 ± 0.14	+0.05 ± 0.14	+0.06 ± 0.13
Weighted mean and error	−0.01 ± 0.03	+0.00 ± 0.04	−0.05 ± 0.03	−0.06 ± 0.03	+0.01 ± 0.03	+ 0.02 ± 0.03	−0.03 ± 0.03
Weighted mean and error of 7 exposures				−0.02 ± 0.01			

Table A3. Measured shifts between the 6 individual exposures of HE 0027−1836 observed in 2012 and the combined exposure made out of all 19 exposures.

Regions	EXP14 ($km\,s^{-1}$)	EXP15 ($km\,s^{-1}$)	EXP16 ($km\,s^{-1}$)	EXP17 ($km\,s^{-1}$)	EXP18 ($km\,s^{-1}$)	EXP19 ($km\,s^{-1}$)
3319−3345	−0.32 ± 0.19	+0.03 ± 0.14	+0.02 ± 0.11	+0.03 ± 0.21	−0.14 ± 0.21	+0.03 ± 0.13
3345−3370	−0.05 ± 0.15	−0.01 ± 0.12	−0.11 ± 0.10	−0.07 ± 0.17	−0.21 ± 0.25	+0.08 ± 0.11
3370−3395	−0.11 ± 0.16	−0.09 ± 0.11	−0.12 ± 0.11	+0.08 ± 0.17	+0.01 ± 0.22	+0.18 ± 0.13
3395−3421	+0.06 ± 0.16	+0.02 ± 0.12	+0.04 ± 0.10	−0.07 ± 0.20	−0.38 ± 0.20	−0.05 ± 0.14
3421−3446	+0.09 ± 0.15	−0.18 ± 0.11	−0.01 ± 0.13	−0.04 ± 0.14	+0.19 ± 0.20	+0.08 ± 0.13
3446−3472	−0.18 ± 0.16	−0.07 ± 0.11	+0.13 ± 0.11	−0.08 ± 0.15	+0.06 ± 0.19	+0.19 ± 0.14
3498−3523	−0.18 ± 0.19	+0.20 ± 0.12	−0.10 ± 0.11	−0.02 ± 0.16	+0.08 ± 0.23	+0.11 ± 0.15

Table A3 – *continued*

Regions	EXP14 (km s^{-1})	EXP15 (km s^{-1})	EXP16 (km s^{-1})	EXP17 (km s^{-1})	EXP18 (km s^{-1})	EXP19 (km s^{-1})
3523−3552	+0.17 ± 0.15	−0.01 ± 0.11	−0.11 ± 0.12	−0.08 ± 0.15	+0.11 ± 0.20	+0.32 ± 0.12
3552−3578	+0.04 ± 0.17	+0.00 ± 0.11	−0.11 ± 0.12	−0.05 ± 0.16	+0.05 ± 0.20	+0.40 ± 0.15
3578−3607	+0.16 ± 0.16	+0.00 ± 0.11	−0.02 ± 0.11	−0.22 ± 0.17	+0.37 ± 0.23	+0.18 ± 0.12
3607−3636	+0.21 ± 0.15	−0.12 ± 0.11	+0.00 ± 0.12	+0.08 ± 0.14	+0.19 ± 0.23	+0.40 ± 0.12
3636−3662	+0.06 ± 0.16	+0.03 ± 0.11	+0.14 ± 0.14	+0.09 ± 0.14	−0.15 ± 0.26	+0.17 ± 0.15
3662−3691	+0.24 ± 0.11	−0.10 ± 0.08	+0.07 ± 0.09	−0.05 ± 0.11	+0.32 ± 0.17	+0.35 ± 0.08
3691−3719	−0.11 ± 0.17	+0.06 ± 0.11	−0.08 ± 0.13	+0.04 ± 0.14	−0.07 ± 0.23	+0.14 ± 0.13
3719−3750	+0.27 ± 0.15	+0.04 ± 0.10	+0.25 ± 0.13	−0.05 ± 0.14	+0.21 ± 0.21	+0.19 ± 0.12
3750−3780	+0.00 ± 0.16	+0.07 ± 0.11	+0.01 ± 0.13	+0.09 ± 0.16	−0.12 ± 0.22	+0.30 ± 0.13
Weighted mean and error	+0.05 ± 0.04	−0.02 ± 0.03	+0.00 ± 0.03	−0.02 ± 0.04	+0.05 ± 0.05	+0.20 ± 0.03
Weighted mean and error of 6 exposures			0.04 ± 0.01			

APPENDIX B: LABORATORY WAVELENGTH OF THE CHOSEN H_2 LINE ALONG WITH THE BEST-FITTING REDSHIFTS FROM THE VOGIT PROFILE ANALYSIS

Table B1. Laboratory wavelength of the set of H_2 transitions that are fitted along with the best redshift and errors from Vogit profile analysis. The uncontaminated (CLEAN) H_2 lines are highlighted in bold letters.

Line ID	Lab wavelength[a] (Å)	Redshift	Velocity (km s^{-1})	K coefficient[b]
L10R0	**981.4387**	**2.401 853(049)**	**+0.35 ± 0.44**	**+0.041**
L7R0	**1012.8129**	**2.401 850(047)**	**+0.07 ± 0.42**	**+0.031**
L3R0	**1062.8821**	**2.401 843(019)**	**−0.55 ± 0.17**	**+0.012**
L2R0	1077.1387	2.401 845(016)	−0.41 ± 0.14	+0.006
L1R0	**1092.1952**	**2.401 846(017)**	**−0.32 ± 0.16**	**−0.001**
L0R0	**1108.1273**	**2.401 845(013)**	**−0.36 ± 0.12**	**−0.008**
L9R1	992.0163	2.401 855(055)	+0.47 ± 0.49	+0.038
L9P1	**992.8096**	**2.401 853(038)**	**+0.30 ± 0.34**	**+0.037**
L8R1	**1002.4520**	**2.401 854(037)**	**+0.43 ± 0.33**	**+0.034**
W0Q1	1009.7709	2.401 845(041)	−0.43 ± 0.36	−0.006
L7R1	1013.4369	2.401 854(047)	+0.43 ± 0.42	+0.030
L7P1	**1014.3272**	**2.401 848(033)**	**−0.16 ± 0.29**	**+0.030**
L5R1	**1037.1498**	**2.401 851(033)**	**+0.14 ± 0.29**	**+0.021**
L4R1	**1049.9597**	**2.401 849(029)**	**+0.01 ± 0.26**	**+0.016**
L4P1	**1051.0325**	**2.401 848(034)**	**−0.14 ± 0.30**	**+0.016**
L2R1	1077.6989	2.401 850(018)	+0.07 ± 0.17	+0.005
L2P1	**1078.9254**	**2.401 846(010)**	**−0.28 ± 0.09**	**+0.004**
L1R1	**1092.7324**	**2.401 848(018)**	**−0.14 ± 0.16**	**−0.001**
L1P1	**1094.0519**	**2.401 850(016)**	**+0.08 ± 0.15**	**−0.003**
L0R1	1108.6332	2.401 850(013)	+0.03 ± 0.12	−0.008
L10R2	**983.5911**	**2.401 855(054)**	**+0.53 ± 0.48**	**+0.039**
L10P2	**984.8640**	**2.401 855(046)**	**+0.53 ± 0.41**	**+0.038**
W1R2	**986.2440**	**2.401 852(035)**	**+0.26 ± 0.32**	**+0.006**
W1Q2	**987.9745**	**2.401 858(032)**	**+0.75 ± 0.29**	**+0.004**
L9P2	994.8740	2.401 851(039)	+0.13 ± 0.35	+0.035
L8R2	**1003.9854**	**2.401 862(035)**	**+1.08 ± 0.32**	**+0.033**
L8P2	**1005.3931**	**2.401 854(041)**	**+0.39 ± 0.37**	**+0.031**
W0R2	1009.0249	2.401 856(035)	+0.62 ± 0.32	−0.005
L5R2	**1038.6902**	**2.401 852(016)**	**+0.27 ± 0.15**	**+0.020**
L5P2	1040.3672	2.401 853(070)	+0.34 ± 0.62	+0.019
L4R2	1051.4985	2.401 851(031)	+0.12 ± 0.28	+0.015
L4P2	**1053.2842**	**2.401 850(029)**	**+0.08 ± 0.26**	**+0.013**
L3R2	1064.9948	2.401 849(016)	−0.01 ± 0.15	+0.010
L2R2	**1079.2254**	**2.401 849(010)**	**−0.04 ± 0.09**	**+0.004**
L2P2	**1081.2660**	**2.401 848(010)**	**−0.15 ± 0.09**	**+0.002**
L1R2	**1094.2446**	**2.401 845(022)**	**−0.41 ± 0.20**	**−0.003**
L10R3	985.9628	2.401 842(053)	−0.63 ± 0.47	+0.036
L10P3	**987.7688**	**2.401 852(035)**	**+0.21 ± 0.31**	**+0.035**
L8R3	1006.4141	2.401 844(070)	−0.44 ± 0.62	+0.030
W0Q3	**1012.6796**	**2.401 850(040)**	**+0.04 ± 0.35**	**−0.009**

Table B1 – *continued*

Line ID	Lab wavelength[a] (Å)	Redshift	Velocity (km s^{-1})	K coefficient[b]
W0P3	**1014.5042**	**2.401 853(029)**	**+0.32 ± 0.26**	**−0.011**
L5R3	**1041.1588**	**2.401 850(020)**	**+0.08 ± 0.18**	**+0.018**
L4R3	1053.9761	2.401 856(042)	+0.56 ± 0.37	+0.013
L4P3	**1056.4714**	**2.401 852(016)**	**+0.26 ± 0.15**	**+0.011**
L3P3	1070.1408	2.401 855(028)	+0.48 ± 0.25	+0.005
L2R3	1081.7112	2.401 853(052)	+0.31 ± 0.46	+0.001
L2P3	**1084.5603**	**2.401 857(019)**	**+0.63 ± 0.17**	**−0.001**
L1P3	**1099.7872**	**2.401 849(023)**	**−0.01 ± 0.20**	**−0.008**
W1Q4	992.0508	2.401 857(076)	+0.68 ± 0.67	−0.000
W1P4	994.2299	2.401 849(052)	+0.00 ± 0.46	−0.002
L9R4	999.2715	2.401 859(068)	+0.88 ± 0.61	+0.030
L9P4	**1001.6557**	**2.401 858(067)**	**+0.77 ± 0.60**	**+0.028**
L8R4	1009.7196	2.401 845(068)	−0.39 ± 0.60	+0.027
L6P4	**1035.1825**	**2.401 847(052)**	**−0.19 ± 0.46**	**+0.017**
L5R4	**1044.5433**	**2.401 853(042)**	**+0.33 ± 0.38**	**+0.014**
L4R4	1057.3807	2.401 858(038)	+0.75 ± 0.34	+0.009
L4P4	**1060.5810**	**2.401 854(046)**	**+0.38 ± 0.41**	**+0.007**
L3P4	**1074.3129**	**2.401 845(033)**	**−0.35 ± 0.29**	**+0.001**
L2R4	**1085.1455**	**2.401 851(037)**	**+0.16 ± 0.33**	**−0.002**
L2P4	**1088.7954**	**2.401 850(033)**	**+0.06 ± 0.29**	**−0.005**
L1P4	**1104.0839**	**2.401 849(077)**	**−0.04 ± 0.68**	**−0.012**
W1Q5	994.9244	2.401 857(063)	+0.64 ± 0.56	−0.003
W0R5	**1014.2425**	**2.401 862(065)**	**+1.11 ± 0.58**	**+0.000**
L8P5	**1017.0043**	**2.401 858(086)**	**+0.80 ± 0.77**	**+0.020**
W0Q5	**1017.8315**	**2.401 855(054)**	**+0.47 ± 0.48**	**−0.014**
L6P5	1040.0587	2.401 853(073)	+0.29 ± 0.64	+0.012
L5P5	**1052.4970**	**2.401 854(095)**	**+0.42 ± 0.84**	**+0.007**
L4R5	**1061.6972**	**2.401 852(062)**	**+0.22 ± 0.55**	**+0.005**
L3R5	**1075.2441**	**2.401 861(069)**	**+1.02 ± 0.61**	**+0.000**
L3P5	1079.4004	2.401 845(062)	−0.38 ± 0.55	−0.003
L2P5	**1093.9550**	**2.401 860(119)**	**+0.96 ± 1.06**	**−0.010**

Column (1): name of the H_2 fitted transitions. Column (2): the laboratory wavelengths. Columns (2) and (3): the best-fitting redshifts for H_2 lines and their errors. Column (5): velocity offset between the redshift of a given H_2 transition and the weighted mean redshift of the all the H_2 lines. Column (6) sensitivity coefficient of H_2 lines.

[a] Wavelengths are from Bailly et al. (2010).

[b] K coefficient are from Ubachs et al. (2007).

APPENDIX C: RESULTS OF VOIGT PROFILE FITTING ANALYSIS FOR DIFFERENT H_2 *J*-LEVELS

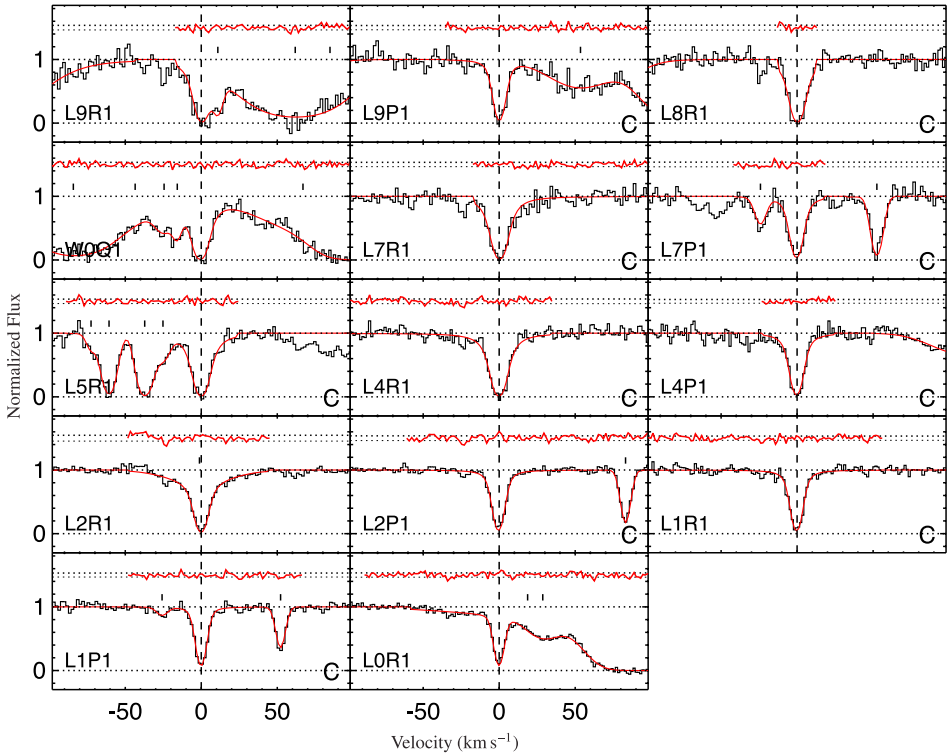

Figure C1. The absorption profiles of H_2 transitions with $J = 1$ in HE 0027−1836 and the best-fitting Voigt profile to the combined spectrum of all exposures after excluding EXP19. The normalized residual (i.e. ([data]−[model])/[error]) for each fit is shown in top of each panel along with the 1σ horizontal line. The vertical ticks mark the positions of fitted contamination.

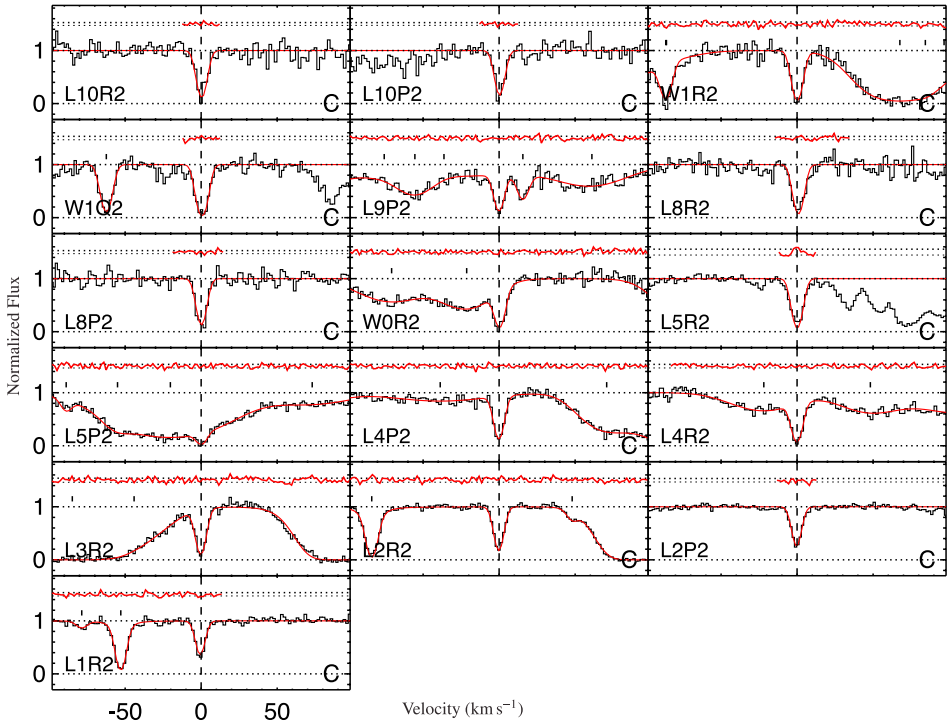

Figure C2. The absorption profiles of H_2 transitions with $J = 2$ in HE 0027−1836 and the best-fitting Voigt profile to the combined spectrum of all exposures after excluding EXP19. The normalized residual (i.e. ([data]−[model])/[error]) for each fit is shown in top of each panel along with the 1σ horizontal line. The vertical ticks mark the positions of fitted contamination.

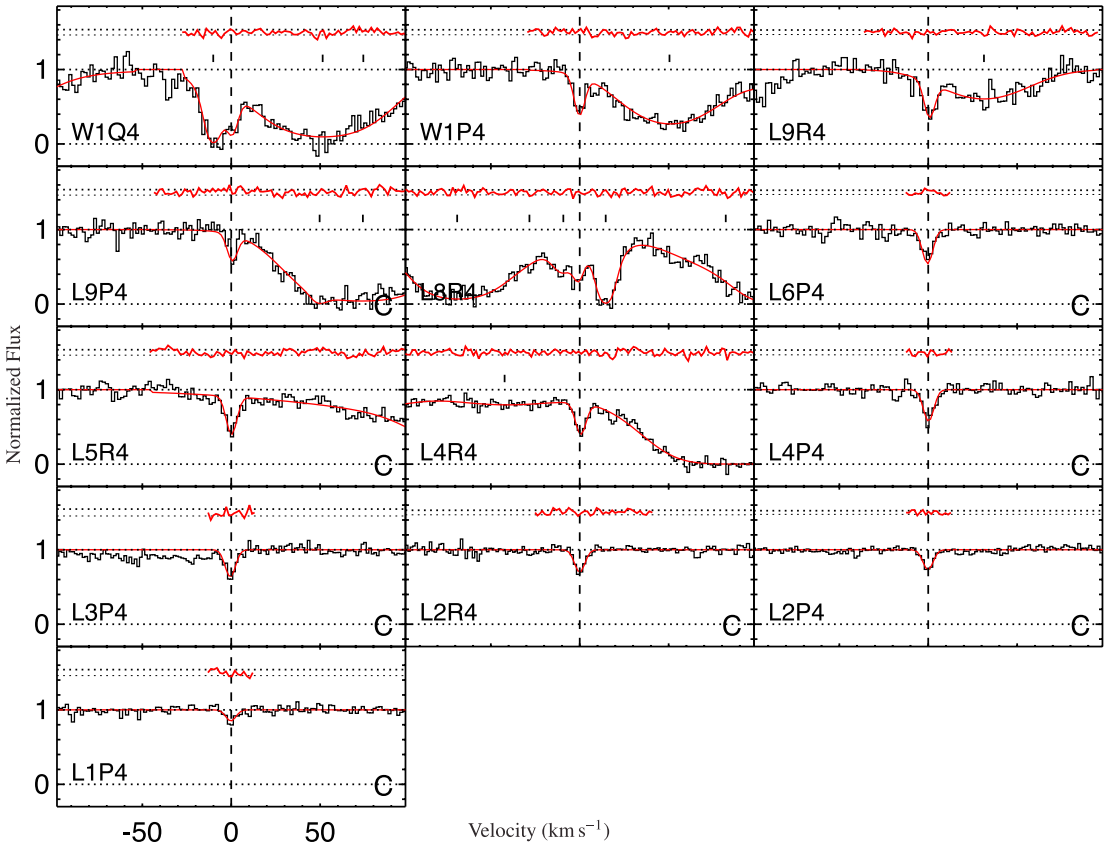

Figure C3. The absorption profiles of H_2 transitions with $J = 4$ in HE 0027−1836 and the best-fitting Voigt profile to the combined spectrum of all exposures after excluding EXP19. The normalized residual (i.e. ([data]−[model])/[error]) for each fit is shown in top of each panel along with the 1σ horizontal line. The vertical ticks mark the positions of fitted contamination.

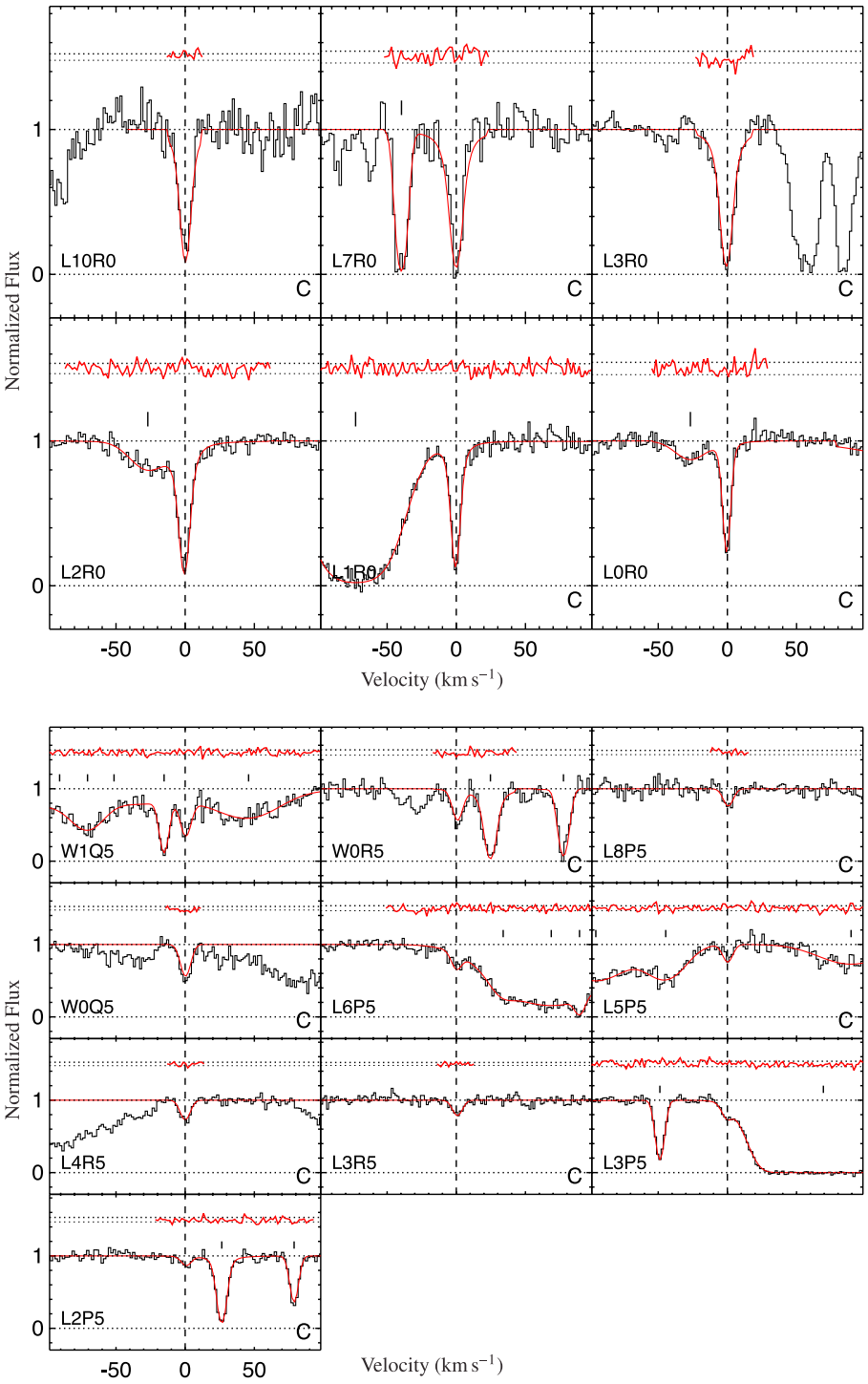

Figure C4. The absorption profiles of H_2 transitions with $J = 0$ (top) and $J = 5$ (bottom) in HE 0027−1836 and the best-fitting Voigt profile to the combined spectrum of all exposures after excluding EXP19. The normalized residual (i.e. ([data]−[model])/[error]) for each fit is shown in top of each panel along with the 1σ horizontal line. The vertical ticks mark the positions of fitted contamination.

This paper has been typeset from a TEX/LATEX file prepared by the author.